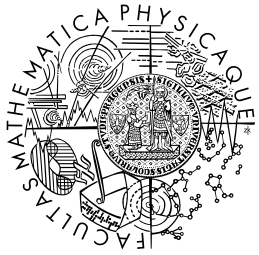

FACULTY
OF MATHEMATICS
AND PHYSICS
Charles University

MASTER THESIS

Jindřich Pipek

Charge transport in semiconducting radiation detectors

Institute of Physics of Charles University

Supervisor of the master thesis:	doc. Ing. Eduard Belas, CSc.
Study programme:	Physics
Study branch:	Optics and Optoelectronics

Prague 2018

I declare that I carried out this master thesis independently, and only with the cited sources, literature and other professional sources.

I understand that my work relates to the rights and obligations under the Act No. 121/2000 Sb., the Copyright Act, as amended, in particular the fact that the Charles University has the right to conclude a license agreement on the use of this work as a school work pursuant to Section 60 subsection 1 of the Copyright Act.

In ..... date ..... signature of the author

Title: Charge transport in semiconducting radiation detectors

Author: Jindřich Pipek

Institute: Institute of Physics of Charles University

Supervisor: doc. Ing. Eduard Belas, CSc., Institute of Physics of Charles University

Abstract: This thesis is focused on study of charge transport in semiconducting radiation detectors. Theoretical calculations of current waveforms based on continuity equation and drift-diffusion equation are done. Useful approximations of current waveforms for detector with shallow electron trap are discussed. Monte Carlo simulation of the current waveforms is proposed and applied to fit experimental current waveforms measured using laser-induced transient current technique and for evaluation of charge transport parameters of the detector such as electric field profile, trapping and detrapping time of traps, drift mobility and other parameters. Detectors prepared from semi-insulating GaAs and CdZnTe single crystals are tested using electrical, spectroscopic and optical characterization techniques.

Keywords: GaAs, CdZnTe, Transient current technique, Monte Carlo simulation of charge transport, radiation detector

I would like to thank all people from the Department of Optoelectronics and Magneto-optics at Institute of Physics of Charles University for friendly and motivating working environment. Foremost, I would like to thank my supervisor Assoc. Prof. Eduard Belas for his guidance and help with measurements during my bachelor and master study. I am also grateful to Prof. Roman Grill for theoretical discussions and inspiring ideas. Immense gratitude belongs to my parents for their help and encouragement in everything I do.

Contents

1. Introduction

1.1 Motivation

The information age, in which we now live, relies on computers and electronic devices based on semiconductors. The discovery of semiconductors in 20th century caused technological revolution from transistor to semiconductor laser. Semiconductors now have many applications one of them are radiation detectors, which can directly convert radiation to electric signal thus having superior energy resolution compared to other radiation detectors like scintillators. Another advantage is short charge collection time, which is affected by drift mobility and distance of electrodes. The quality of the detector depends on its preparation and transport properties of used material. An enormous effort was taken to understand the principles of charge transport. Many approaches were found from which one uses drift-diffusion equation in combination with continuity equation to model charge transport. Standard experimental methods for testing radiation detectors such as spectroscopic measurement gives only information about collected charge, which is proportional to the energy of detected radiation and applied bias [1]. This type of measurement gives no information about charge dynamics, which is needed to distinguish the contribution of charge trapping and space charge effect. More advanced method has to be used for investigation of the detector performance.

1.2 Transient Current Technique

One of the powerful methods to study charge transport in semiconductors is Transient Current Technique (TCT), which belongs to the family of Time-of-Flight methods based on measuring current response of the semiconductor detector to the external event (impact of alpha particle, electron, laser pulse, etc.) generating electron-hole (e-h) pairs near under the bombarded electrode [2]. Since TCT gives a current dependence on time, much more information about charge transport can be obtained. For example internal electric field, drift mobility, charge collection efficiency (CCE) and parameters of trap levels. Laser-induced Transient Current Technique (L-TCT) is based on above band-gap laser pulse used as an external source generating e-h pairs. Possibility of triggering on laser pulse significantly decreases noise compared to untriggered sources like alpha particle. L-TCT is the main method used in the experimental part of this thesis to obtain detector transport properties.

1.3 Basic properties of GaAs and CdZnTe

One of the materials suitable for radiation detection are Gallium Arsenide (GaAs) and Cadmium Zinc Telluride (CdZnTe). GaAs is III-V compound semiconductor with direct band-gap, which crystallizes in zinc-blende structure (see figure 1.1). GaAs is studied for more than 40 years and has many applications such as microwave frequency integrated circuits, solar cells and laser diodes [3]. The preparation of high quality detector grade material was not possible until recently. New semiinsulating chromium compensated GaAs single crystals suitable for radiation detection recently appeared [4]. Selected properties of GaAs are shown in table 1.1. CdZnTe is II-VI compound semiconductor with direct band-gap, which crystallizes in zinc-blende structure (see figure 1.1). CdZnTe has chemical formula $Cd_{1-x}Zn_xTe$ where x $\approx$ 0.1 for material used in this work). It is the state of the art material for radiation detection because it has high atomic number resulting in high probability of photoelectric effect, high density giving it high absorption coefficient, high resistivity and wide band-gap, which allow CdZnTe to operate at room temperature. Selected properties of CdZnTe are shown in table 1.1.

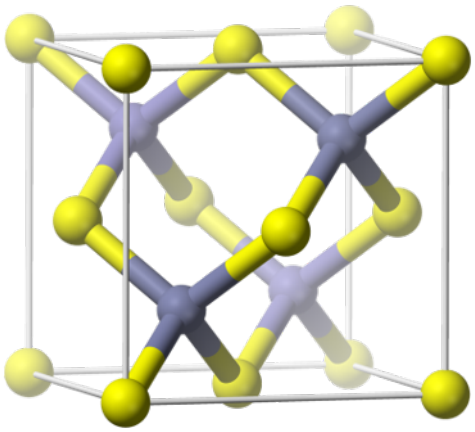

Figure 1.1: Zinc-blende crystal structure

Table 1.1: Properties of GaAs and CdZnTe at room temperature [5].

Material	GaAs	$Cd_{0.9}Zn_{0.1}Te$
Atomic number	31, 33	48, 30, 52
Density (g/cm^3)	5.32	6.2
Band-gap (eV)	1.43	1.5
e-h pair production energy (eV)	4.2	4.43
Resistivity (Ωcm)	10^8	10^{11}
Electron mobility μ_e (cm^2/Vs)	8000	1100
Hole mobility μ_h (cm^2/Vs)	400	100

1.4 The goal of this thesis

This thesis is focused on the development of fast and reliable method for characterization of detector-grade material and the quality of prepared detectors. Several authors have reported theoretical calculations for special configurations of a detector with trap centers without space charge effects [6], [7], [8]. Examples of analytic solution of drift-diffusion equation are shown in chapter 2. Analytic solutions are important for the insight into properties of current waveforms and for comparison with numerical methods. To study current waveforms of detector with more than one trap level and space charge effects, numerical methods must be used. Complete numerical solution of one dimensional (1D) drift-diffusion equation and Poisson equation is given in [9]. These calculations are slow and not useful for fast exploration of possible parameter values needed to fit experimental data. In this thesis Monte Carlo (MC) simulation of 1D charge transport is proposed. This simulation is based on the concept shown in [10]. Goal of this thesis is to expand mentioned concept to include arbitrary internal electric field profile, effects of diffusion, wavelength of excitation laser pulse and other parameters (see chapter 3). Proposed MC simulation is verified using analytical solution and applied to fit experimental L-TCT data for GaAs and CdZnTe detectors from which transport parameters are found (see chapter 5).

2. Theory

2.1 Charge transport equations

When treating the charge transport phenomena in semiconductor detectors it is useful to start with the continuity equation

$$\frac{\partial n}{\partial t} = \frac{1}{e}\nabla \cdot \vec{j_e} + GR, \tag{2.1}$$

where n is the concentration of electrons in the conduction band, e is the elementary charge, $\vec{j_e}$ is the electron current density and GR represents the electron generation and recombination. Electron current density can be evaluated from the drift-diffusion equation for constant temperature

$$\vec{j_e} = en\mu_e\vec{\mathcal{E}} + eD_e\nabla n, \tag{2.2}$$

where the first term is a drift part and the second is a diffusion part, μ_e is the electron mobility, $\vec{\mathcal{E}}$ is the electric field intensity and D_e is the diffusion coefficient for electrons related to mobility by the Einstein relation

$$D_e = \frac{k_B\mathcal{T}}{e}\mu_e, \tag{2.3}$$

where k_B is Boltzmann constant and $\mathcal{T}$ is the absolute temperature [11]. Analogical equations for holes can be found letting $e \to -e$, $\mu_e \to -\mu_h$.

2.2 Assumptions

We assume throughout the all text that the detector is rectangular with two planar opposite electrodes with the distance L between them. Next assumption is that the size of electrodes is much greater than L, which allows us to simplify calculations by working only in one spatial dimension which is parallel with electric field and labeled as x-coordinate. The irradiated area on the electrode is near its center so the electric field is homogeneous across the area and perpendicular to it. Described detector geometry is shown in figure 2.1.

Another assumption is that drift mobility μ is space and time independent. Electrons are considered noninteracting and photogenerated charge is small so its effect on the electric field is neglected. We use sign convention,

$$\vec{j} = -j\hat{x}, \quad \vec{\mathcal{E}} = -\mathcal{E}\hat{x}, \quad \mathcal{E} = \frac{\mathrm{d}\varphi}{\mathrm{d}x}, \tag{2.4}$$

where $\hat{x}$ is the unit vector in the direction of x-axis, $\vec{j}$ is the current density, $j = \left|\vec{j}\right|$, $\vec{\mathcal{E}}$ is the electric field intensity, $\mathcal{E} = \left|\vec{\mathcal{E}}\right|$ and $\varphi(x)$ is the electric potential [12]. All formulas are calculated for electrons only, for holes analogical formulas can be found. For the simplification of later used formulas we define the boxcar function $\chi_{[0,x_1]}(x)$

$$\chi_{[0,x_1]}(x) = \Theta(x) - \Theta(x - x_1) = \begin{cases} 1 & 0 \le x \le x_1 \\ 0 & \text{otherwise,} \end{cases} \tag{2.5}$$

where $\Theta(x)$ is the Heaviside unit step function

$$\Theta(x) = \begin{cases} 0 & x < 0 \\ 1 & x \geq 0. \end{cases} \tag{2.6}$$

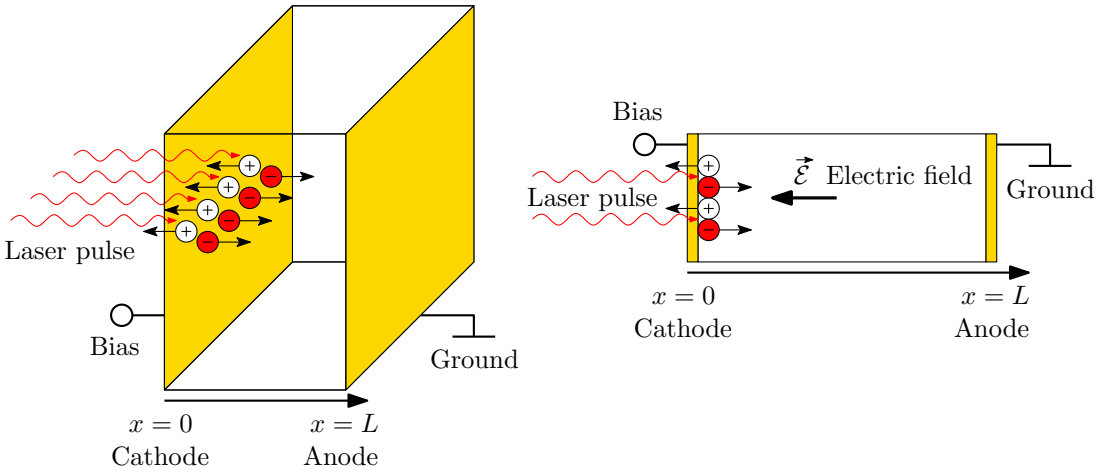

Figure 2.1: **Left**: Scheme of the detector with two planar electrodes which are depicted with gold color. **Right**: 1D model of detector, where electrons and holes can move only along x-axis. The vertical dimension is only for visualization of electrons and holes.

2.3 Shockley-Ramo theorem

A single carrier moving a distance Δx between two parallel electrodes, in a direction parallel to the electric field induces, at the electrodes, a charge ΔQ given by [13]

$$\Delta Q = e\frac{\Delta x}{L}, \tag{2.7}$$

where L is the distance between electrodes. The total induced current $I(t)$ (also called current waveform) is the time derivative of (2.7) summed over all drifting carriers

$$I(t) = \frac{Q(t)v(t)}{L}, \tag{2.8}$$

where Q is the moving charge and v is the velocity of the moving charge. The equation (2.8) is a special case of the Shockley-Ramo theorem [14] for the geometry described in section 2.2. The equation (2.8) can be generalized for different electrodes configuration [14].

2.4 Charge drift

If the electric field intensity is constant $\mathcal{E}(x) = \mathcal{E}_0$, then the drift velocity $v_0 = \mu_e\mathcal{E}_0$ is constant and if we neglect the charge generation-recombination $GR = 0$ and the diffusion $D_e = 0$, then from (2.1) and (2.2) we get simple one dimensional transport equation

$$\frac{\partial n(x,t)}{\partial t} = -v_0\frac{\partial n(x,t)}{\partial x}. \tag{2.9}$$

Solution of (2.9) is

$$n(x,t) = n_0(x - v_0t), \tag{2.10}$$

where $n_0(x)$ is the initial charge distribution [15]. The expression in (2.10) simply states that the initial electron cloud $n_0(x)$ moves with the constant drift velocity v_0. In this case no changes of electron cloud shape occur. Let's assume the detector with two planar opposite electrodes with the distance L between them. In $t = 0$ sharply localized photogenerated electron cloud at the cathode ($x = 0$) is

$$n_0(x) = \mathcal{N}_0\delta(x), \tag{2.11}$$

where $\mathcal{N}_0$ is the initial number of electrons in the conduction band and $\delta(x)$ is the Dirac delta function. The time evolution of $n(x,t)$ is from (2.10)

$$n(x,t) = \mathcal{N}_0\delta(x - v_0t)\chi_{[0,L]}(x), \tag{2.12}$$

where boxcar function $\chi_{[0,L]}(x)$ represents charge collection at the cathode $x = 0$ and the anode $x = L$. Electron cloud $n(x,t)$ drifts through the detector with its center $x_C(t) = v_0t$ moving with constant drift velocity, until the cloud arrives at the collecting electrode $x_C(T_R) = L$ in time T_R called the default transit time, which is defined by

$$T_R = \frac{L}{v_0} = \frac{L}{\mu_e\mathcal{E}_0} = \frac{L^2}{\mu_eU}, \tag{2.13}$$

where $U = \mathcal{E}_0L$ is the applied bias. The default transit time T_R is used in all text as comparative time even for detectors where the mentioned assumptions might

not hold. We shall also define actual transit time t_r or simply transit time, which includes effects of varying electric field in the detector, detrapping phenomena and diffusion, which might be different form T_R. The total moving charge $Q(t)$ is given by

$$Q(t) = -e \int n(x,t) \mathrm{d}x, \tag{2.14}$$

and using (2.12) we get

$$Q(t) = -e\mathcal{N}_0 \chi_{[0,T_R]}(t) = Q_0 \chi_{[0,T_R]}(t), \tag{2.15}$$

where $Q_0 = -e\mathcal{N}_0$ is the initial photogenerated charge. It is important to note that the integral of the delta function $\delta(x - v_0 t)$ is nonzero for $t \in [0, T_R]$ (which follows from $T_R = L/v_0$). The boxcar $\chi_{[0,T_R]}(t)$ in (2.15) represents the collection of charge in time domain. From the Shockley-Ramo theorem (2.8) using (2.13) and (2.15) the current response to the electron cloud movement is

$$I(t) = \frac{Q(t)v_0}{L} = \frac{Q_0}{T_R} \chi_{[0,T_R]}(t) = I_0 \chi_{[0,T_R]}(t), \tag{2.16}$$

where $I_0 = \frac{Q_0}{T_R}$ is the default current amplitude, which will be used through the text to normalize current waveforms in graphs. The electron drift and normalized current waveforms are illustrated in the figure 2.2. Initially in $t = 0$ the electron cloud $n_0(x) \propto \delta(x)$ is the delta function and drifts in the constant electric field to the anode $x = L$ for time T_R. Electron cloud (2.11) is a convenient approximation of a localized electron cloud, which is near under the cathode and has the full width at half maximum FWHM $\ll L$. Current waveform (2.16) can be generalized to include absorption profile of generating laser pulse, as a convolution of solution for $\delta(x)$ (2.16) and Lambert-Beer law

$$I_l(x) = I_{l0} \exp(-\alpha x), \tag{2.17}$$

where I_l, I_{l0} is the light intensity and α is the absorption coefficient.

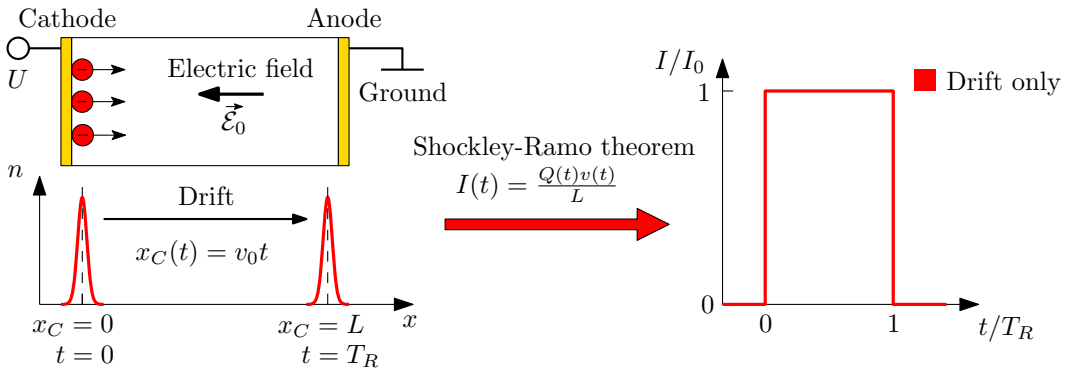

Figure 2.2: **Left**: Scheme of the detector and the electron cloud. Electrons drift through the bulk towards the anode with drift velocity $v_0 = \mu_e \mathcal{E}_0$. **Left bottom**: Electron concentration at $t = 0$ and $t = T_R$ is represented by red Gaussian approximation curve. **Right**: Normalized current waveform, which is related to the motion of charge carriers via the Shockley-Ramo theorem.

2.5 Charge transport with diffusion

In case of diffusion $D_e \neq 0$, and if we neglect the charge generation-recombination $GR = 0$, we get from (2.1) and (2.2) equation

$$\frac{\partial n(x,t)}{\partial t} = -v_0 \frac{\partial n(x,t)}{\partial x} + D_e \frac{\partial^2 n(x,t)}{\partial x^2}. \tag{2.18}$$

This equation is a special case of Einstein-Kolmogorov equation for Brownian motion with constant diffusion coefficient and drift velocity [15]. The solution of equation (2.18) is found by coordinate transform

$$X = x - v_0 t \tag{2.19}$$

$$T = t. \tag{2.20}$$

Partial derivatives in (2.18) can be rewritten using (2.19),(2.20) and the chain rule to

$$\frac{\partial}{\partial x} = \frac{\partial}{\partial X}\frac{\partial X}{\partial x} + \frac{\partial}{\partial T}\frac{\partial T}{\partial x} \tag{2.21}$$

$$\frac{\partial}{\partial t} = \frac{\partial}{\partial X}\frac{\partial X}{\partial t} + \frac{\partial}{\partial T}\frac{\partial T}{\partial t}, \tag{2.22}$$

equation (2.18) becomes diffusion equation

$$\frac{\partial n(X,T)}{\partial T} = D_e \frac{\partial^2 n(X,T)}{\partial X^2}, \tag{2.23}$$

which has Green's function [15]

$$G(X,T) = \left(\frac{1}{4\pi D_e T}\right)^{1/2} \exp\left(-\frac{(X)^2}{4D_e T}\right) \Theta(T). \tag{2.24}$$

Transforming Green's function (2.24) backwards from X, T to x, t gives

$$G(x,t) = \left(\frac{1}{4\pi D_e t}\right)^{1/2} \exp\left(-\frac{(x - v_0 t)^2}{4D_e t}\right) \Theta(t), \tag{2.25}$$

which is the final Green's function for equation (2.18), where the second term is the Gaussian function with its center $x - v_0 t$ moving with constant velocity v_0. General solution of (2.18) is equal to a convolution of Green function $G(x,t)$ and initial electron cloud $n(x,t)$ [15]

$$n(x,t) = G * n_0(x) = \int_{-\infty}^{+\infty} G(x - y, t) n_0(y) \mathrm{d}y. \tag{2.26}$$

If the initial electron cloud is the delta function $n_0(x) = \mathcal{N}_0 \delta(x)$ then the solution of (2.18) is the Green function itself since the delta function acts as identity in convolution. Electron cloud is then

$$n(x,t) = \mathcal{N}_0 \, \Theta(t) \left(\frac{1}{4\pi D_e t}\right)^{1/2} \exp\left(-\frac{(x - v_0 t)^2}{4D_e t}\right) \chi_{[0,L]}(x), \tag{2.27}$$

where the boxcar function $\chi_{[0,L]}(x)$ represents the charge collection at the cathode $x = 0$ and the anode $x = L$. The current is obtained in analogical way to section 2.4.

$$I(t) = \frac{Q_0}{T_R}\,\Theta(t)\left(\frac{1}{4\pi D_e t}\right)^{1/2}\int_0^L \exp\left(-\frac{(x - v_0 t)^2}{4D_e t}\right)\mathrm{d}x. \tag{2.28}$$

Integral of the Gaussian function is the Error function defined as

$$\operatorname{erf}(x) = \frac{2}{\sqrt{\pi}}\int_0^x \exp\left(-s^2\right)\mathrm{d}s. \tag{2.29}$$

Error function is an odd function and is constrained by a pair of horizontal asymptotes $y = \pm 1$, which is shown in the figure 2.3. With this function the current (2.28) can be analytically computed

$$I(t) = \frac{Q_0}{T_R}\,\Theta(t)\frac{1}{2}\left[\operatorname{erf}\left(\frac{L - v_0 t}{\sqrt{4Dt}}\right) + \operatorname{erf}\left(\frac{v_0 t}{\sqrt{4Dt}}\right)\right]. \tag{2.30}$$

Center of the electron cloud $x_C = v_0 t$ moves with the velocity $v_0 = \mu_e \mathcal{E}_0$. The electron cloud itself broadens, which is caused by diffusion. Diffusion smears the transient edge but leaves the transit time t_r same as the default transit time T_R, which correspond to arrival of the center of the electron cloud x_C. The transport and diffusion of electron cloud is illustrated in figure 2.4. The current waveform (2.30) is similar to (2.16) for carrier drift, except the boxcar function $\chi_{[0,T_R]}(t)$ in (2.16) is replaced with the sum of two Error functions in (2.30). The current waveform (2.30) is correct for $t \gg 0$ when the electron cloud drifted to the anode and is far from the cathode. For time $t \approx 0$, some electrons might diffuse to the cathode and recombine there. This effect can be included into the model of surface recombination, which is described in section 2.9. Diffusion has to be included to the analysis of all current waveforms for precise determination of transport parameters (transit time, etc.). However, in the following sections, diffusion will be neglected for simplification of the current waveform analysis, and is included in Monte Carlo simulation presented in chapter 3.

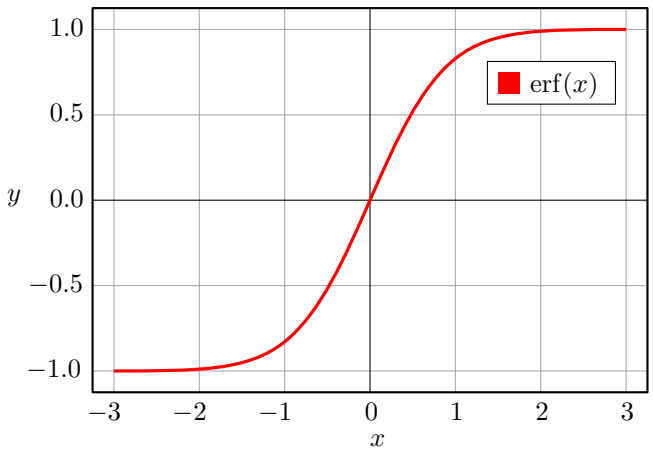

Figure 2.3: Plot of the Error function.

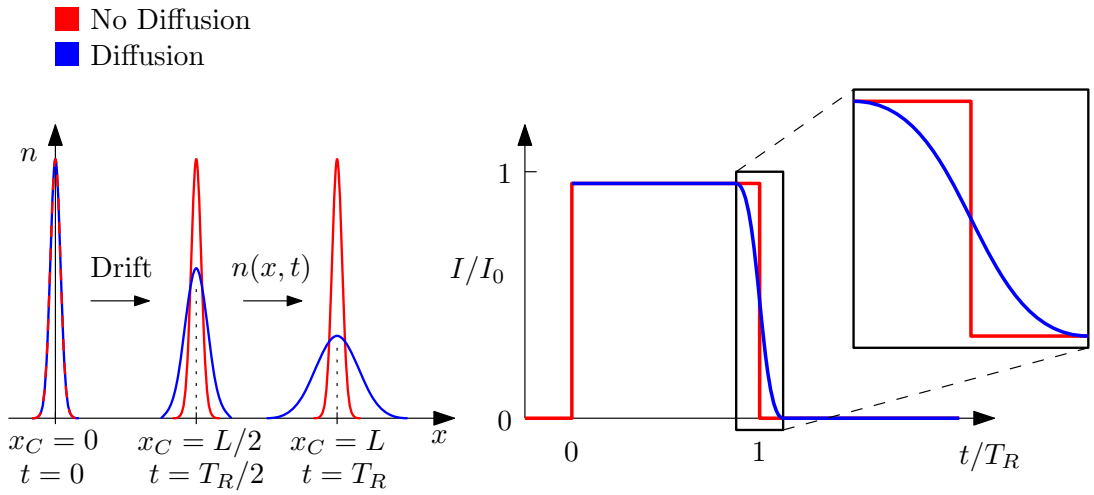

Figure 2.4: **Left**: Evolution of the electron cloud $n(x,t)$. The red curve represents the case with no diffusion and the blue curve is with diffusion. **Right**: Normalized current waveforms for the detector with diffusion included (blue curve) or not included (red curve).

2.6 Charge trapping and detrapping

One of the most critical factors influencing the performance of semiconductor detectors is the presence of trapping centers resulting in decreasing collected charge and dropping resolution of a detector. Trapping process is a process in which an electron (hole) is captured by a center and then has a much greater probability of being thermally re-emitted into the conduction (valence) band than of recombining with a hole (electron) that is captured by the same center [16]. Therefore when a uniform distribution of trapping centers is present inside the material, trapping and detrapping processes can be described by the trapping time τ_T (average time when a carrier is free before it is trapped), and the detrapping time τ_D (average time spent in the trap by a captured carrier before its release). Trapping time and detrapping time are respectively defined as [13]

$$\tau_T = \frac{1}{N_T \sigma_c v_{th}}, \tag{2.31}$$

$$\tau_D = \frac{1}{N_C \sigma_c v_{th}} \exp\left(\frac{E_T}{k_B \mathcal{T}}\right). \tag{2.32}$$

Here N_T is the trap concentration, σ_c the capture cross section, v_{th} the thermal velocity of carrier, N_C the effective density of states in the conduction band, E_T trap energy in the band-gap, k_B is the Boltzmann constant and $\mathcal{T}$ is the absolute temperature of the detector. We assume non-degenerate statistics and that most of the traps remain empty, allowing a constant trapping and detrapping time to be defined [7]. Processes of electron trapping and detrapping in band diagram are depicted in figure 2.5

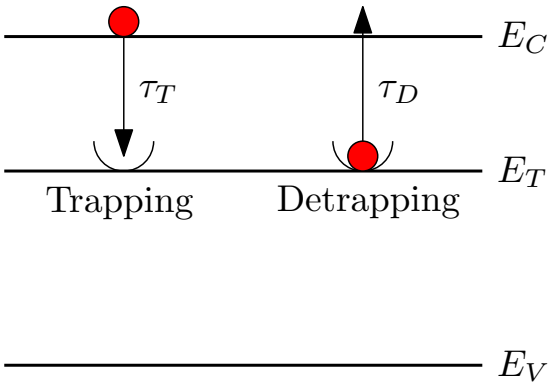

Figure 2.5: Band diagram of electron trap with energy E_T. Processes of trapping and detrapping (marked with arrow) are characterized by the trapping time τ_T and the detrapping time τ_D, respectively.

2.6.1 One shallow and one deep electron trap

Let's assume the detector with one shallow and one deep electron trap level. The trap level with smaller detrapping time is labeled with S and called the shallow trap, in the sense that both trapping and detrapping time τ_{TS}, τ_{DS} are similar or less T_R thus repeated trap-detrap events can occur. The trap level with greater detrapping time is labeled with D and called the deep trap, in the sense that thermal release of captured carriers is not probable in a time interval equal to T_R, this means that $\tau_{DD} \gg T_R$, where τ_{DD} is the detrapping time of the deep trap level. The trapping time of the deep level is labeled τ_{TD}. Important processes of electron trapping and detrapping are depicted in figure 2.6.

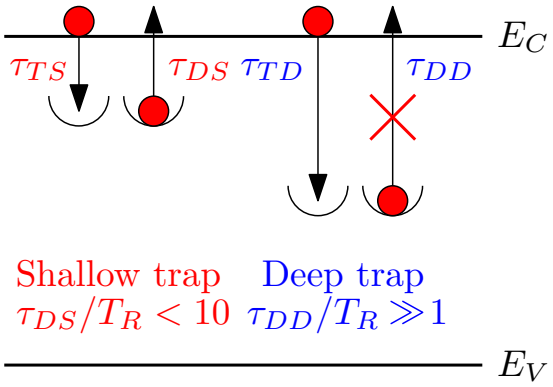

Figure 2.6: Band diagram with shallow and deep trap. Process of trapping and detrapping (marked with arrow) are characterized by the trapping time τ_{TS}, τ_{TD} and the detrapping time τ_{DS}, τ_{DD} respectively. In case of the deep trap, the detrapping time τ_{DD} is much larger than the default transit time T_R and thus detrapping from deep trap is neglected.

Investigation of charge trapping and detrapping was done in [6] where current transients were calculated using continuity equation and Poisson's equation. Our approach is different in direct use of kinetic equations for two level system, which

leads to the solution in easier and more straightforward way. Similar approach when only one trap center is present in the detector was shown in [16]. The kinetic equations for two level model is given for $t < T_R$ by

$$\frac{\mathrm{d}n}{\mathrm{d}t} = -\frac{n}{\tau_{TS}} + \frac{n_S}{\tau_{DS}} - \frac{n}{\tau_{TD}} \tag{2.33}$$

$$\frac{\mathrm{d}n_S}{\mathrm{d}t} = \frac{n}{\tau_{TS}} - \frac{n_S}{\tau_{DS}} \tag{2.34}$$

$$\frac{\mathrm{d}n_D}{\mathrm{d}t} = \frac{n}{\tau_{TD}}, \tag{2.35}$$

where n is the concentration of electrons in the conduction band, n_S is the concentration of electrons in the shallow trap, n_D is the concentration of electrons in the deep trap. For time $t > T_R$ some electrons can be collected on the anode and corresponding term must be added to (2.33) together with spatial dependence, which will be shown in chapter 3. Sum of all three equations (2.33)-(2.35) gives:

$$\frac{\mathrm{d}(n + n_S + n_D)}{\mathrm{d}t} = 0, \tag{2.36}$$

which is a simple statement of conservation of electrons in the detector. Integration of (2.36) yields

$$n + n_S + n_D = const. = n_0, \tag{2.37}$$

where n_0 is the initial concentration of electrons in the detector. Inserting (2.37) into (2.33) gives

$$\frac{\mathrm{d}n}{\mathrm{d}t} + n\left(\frac{1}{\tau_C}\right) = \frac{n_0}{\tau_{DS}} - \frac{n_D}{\tau_{DS}}, \tag{2.38}$$

where

$$\frac{1}{\tau_C} = \frac{1}{\tau_{TS}} + \frac{1}{\tau_{TD}} + \frac{1}{\tau_{DS}}. \tag{2.39}$$

Differentiation of (2.38) with respect to time gives

$$\frac{\mathrm{d}^2 n}{\mathrm{d}t^2} + \frac{\mathrm{d}n}{\mathrm{d}t}\frac{1}{\tau_C} + \frac{\mathrm{d}n_D}{\mathrm{d}t}\frac{1}{\tau_{DS}} = 0, \tag{2.40}$$

and substitution of (2.35) into (2.40) gives

$$\frac{\mathrm{d}^2 n}{\mathrm{d}t^2} + \frac{\mathrm{d}n}{\mathrm{d}t}\frac{1}{\tau_C} + n\frac{1}{\tau_{TD}\tau_{DS}} = 0. \tag{2.41}$$

This is a second order linear homogeneous differential equation that has characteristic equation

$$\Lambda^2 + \frac{1}{\tau_C}\Lambda + \frac{1}{\tau_{TD}\tau_{DS}} = 0. \tag{2.42}$$

This characteristic equation has two roots given by the discriminant formula

$$\Lambda_{1,2} = \frac{-\frac{1}{\tau_C} \pm \sqrt{\frac{1}{\tau_C^2} - 4\frac{1}{\tau_{TD}\tau_{DS}}}}{2}. \tag{2.43}$$

Discriminant in (2.43) is equal to

$$\frac{1}{\tau_C^2} - 4\frac{1}{\tau_{TD}\tau_{DS}} = \frac{1}{\tau_{TS}^2} + 2\left(\frac{1}{\tau_{TS}\tau_{TD}} + \frac{1}{\tau_{TS}\tau_{DS}}\right) + \frac{1}{\tau_{TD}^2} + \frac{1}{\tau_{DS}^2} - \frac{2}{\tau_{TD}\tau_{DS}}, \tag{2.44}$$

where the sum of last three terms in (2.44) is

$$\frac{1}{\tau_{TD}^2}+\frac{1}{\tau_{DS}^2}-\frac{2}{\tau_{TD}\tau_{DS}}=\left(\frac{1}{\tau_{TD}}-\frac{1}{\tau_{DS}}\right)^2\geq 0, \tag{2.45}$$

and thus the discriminant (2.44) is greater than 0, which implies two distinct values of Λ in (2.43). The general solution of (2.41) is

$$n(t)=n_0\left[A\exp\left(\Lambda_1 t\right)+B\exp\left(\Lambda_2 t\right)\right], \tag{2.46}$$

where A and B are determined from initial conditions. In $t=0$ there are no electrons trapped $n_D(0)=0$ and $n_S(0)=0$, from (2.37) which implies $n(0)=n_0$ we get equation

$$A+B=1. \tag{2.47}$$

From (2.38) for $t=0$ with knowledge of $n_D(0)=0$ and from (2.46) it follows

$$A=\frac{1}{2}\left(1+\frac{\frac{1}{\tau_{DS}}-\frac{1}{\tau_t}}{\sqrt{\frac{1}{\tau_C^2}-4\frac{1}{\tau_{TD}\tau_{DS}}}}\right), \tag{2.48}$$

where τ_t is defined by

$$\frac{1}{\tau_t}=\frac{1}{\tau_{TS}}+\frac{1}{\tau_{TD}}. \tag{2.49}$$

B is determined from

$$B=\frac{1}{2}\left(1-\frac{\frac{1}{\tau_{DS}}-\frac{1}{\tau_t}}{\sqrt{\frac{1}{\tau_C^2}-4\frac{1}{\tau_{TD}\tau_{DS}}}}\right), \tag{2.50}$$

It can be shown that

$$\left|\frac{\frac{1}{\tau_{DS}}-\frac{1}{\tau_t}}{\sqrt{\frac{1}{\tau_C^2}-4\frac{1}{\tau_{TD}\tau_{DS}}}}\right|<1, \tag{2.51}$$

from which $A,B\in[0,1]$. It is also important that $\Lambda_{1,2}<0$, which follows directly from (2.43). Thus the solution (2.46) can be rewritten into more useful form

$$n(t)=n_0\left[A\exp\left(-\frac{t}{\tau_1}\right)+B\exp\left(-\frac{t}{\tau_2}\right)\right], \tag{2.52}$$

where τ_1,τ_2 are characteristic times, which are always positive and defined by

$$\tau_1=-\frac{1}{\Lambda_1}\qquad\text{and}\qquad\tau_2=-\frac{1}{\Lambda_2}. \tag{2.53}$$

Solution in form (2.46) or (2.52) has always decreasing slope, which reflects the loss of free charge due to trapping into the deep trap, which on the time scale of T_R doesn't release electrons back to the conduction band. This solution fully describes trapping and detrapping phenomena under mentioned conditions for $0\leq t\leq T_R$. The concentration of electrons in the conduction band $n(t)$ (2.52) is connected to the current waveform $I(t)$ via the Shockley-Ramo theorem (2.8) and using (2.14) we get

$$I(t)=\frac{Q_0}{T_R}\left[A\exp\left(-\frac{t}{\tau_1}\right)+B\exp\left(-\frac{t}{\tau_2}\right)\right], \tag{2.54}$$

which is the desired current waveform for time $0 \leq t \leq T_R$. Normalized current waveforms (2.54) of the detector with the shallow trap $\tau_{TS}/T_R \approx 1/4, \tau_{DS}/\tau_S \approx 1/10$ and the deep trap $\tau_{TD}/T_R \approx 1/10$ is depicted in figure 2.7. For time $t > T_R$ some electrons can be collected on the detector anode and the system of differential equations (2.33)-(2.35) must be changed, analytical solution does not exist and Monte Carlo simulation can be used for current waveform analysis, which is described in chapter 3.

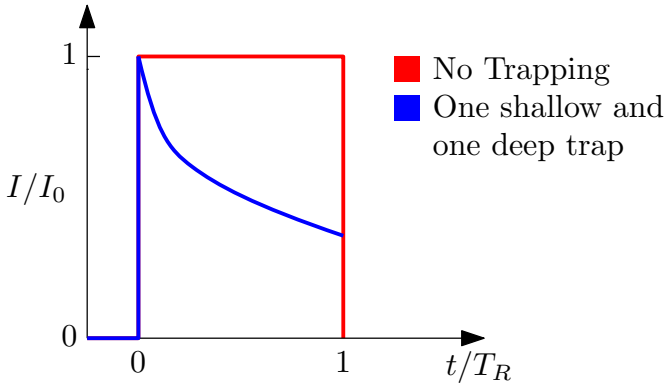

Figure 2.7: Normalized current waveform of the detector with one shallow and one deep trap, which is the sum of two exponential decays (blue curve) and current waveform for the detector without traps, which is a constant function (red curve).

2.6.2 One deep electron trap

Let's assume a detector with only one deep trap with trapping time τ_{TD} and no detrapping (detrapping time $\tau_{DD} \approx +\infty$) [16]. This allows us to write

$$GR = -\frac{n(x,t)}{\tau_{TD}}. \tag{2.55}$$

If we neglect diffusion $D_e = 0$ then from (2.1) and (2.2) using (2.55) we get transport equation with decay:

$$\frac{\partial n(x,t)}{\partial t} = -v_0 \frac{\partial n(x,t)}{\partial x} - \frac{n(x,t)}{\tau_{TD}}. \tag{2.56}$$

General solution of (2.56) $n(x,t)$ is

$$n(x,t) = n_0(x - v_0 t) \exp\left(-\frac{t}{\tau_{TD}}\right) \Theta(t), \tag{2.57}$$

where $n_0(x) = n(x, t = 0)$ is the initial charge distribution. This solution delineates the fact of charge transport with losses due to trapping. The current waveform is obtained in a similar way to the case with charge drift only (see section 2.4), the only difference is that Q_0 in (2.16) is replaced with

$$Q(t) = Q_0 \exp\left(-\frac{t}{\tau_{TD}}\right), \tag{2.58}$$

from which

$$I(t) = \frac{Q_0}{T_R} \exp\left(-\frac{t}{\tau_{TD}}\right) \chi_{[0,T_R]}(t), \tag{2.59}$$

where the only difference from (2.16) is the exponential decay representing the loss of charge due to trapping. The solution (2.59) can be also found as a special case of solution (2.54) for the sample with one shallow and one deep trap in subsection 2.6.1 by letting $\tau_{TS} \to +\infty$. Illustration of current waveforms for several values of τ_{TD} is shown in figure 2.8.

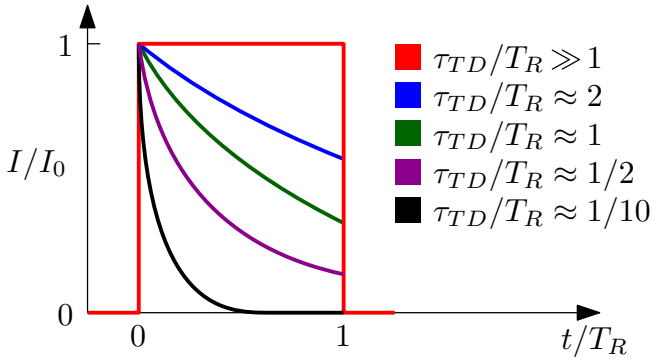

Figure 2.8: Normalized current waveforms of the detector with one deep trap. The red curve is the limit example with no trappping for comparison with the exponential decay of waveforms that ends at $t = T_R$ when the electron cloud is collected.

2.7 Electric field profile

The spatial dependence of the electric field intensity (electric field profile) inside the detector is very important for charge transport since it directly affects the drift velocity. In the most simplified case when the space charge density in the detector $\rho(x) = 0$, the electric field profile is constant $\mathcal{E}(x)$ and space independent inside the detector [17].

2.7.1 Constant space charge

When the the space charge density $\rho(x) = \rho_0$ is constant in the whole detector, the electric field $\mathcal{E}(x)$ can be easily calculated from the Gauss law

$$\oint \vec{D} \cdot \mathrm{d}\vec{A} = Q_s, \tag{2.60}$$

where $\vec{D} = \varepsilon_r \varepsilon_0 \vec{\mathcal{E}}$ is the electric displacement field, ε_0 is the vacuum permittivity, ε_r is the relative permittivity of used material and Q_s is the charge inside the closed surface over which we integrate. If we assume that the size of the detector electrodes is much greater than the distance L between them, we can treat the detector as one dimensional (x-axis). From this geometry, the electric field is perpendicular to electrodes and the only nonzero contribution to the integral in (2.60) is through electrodes. The electric field inside the detector ($0 \leq x \leq L$) is then [17]

$$\mathcal{E}(x) = (-x + \frac{L}{2}) \frac{e\rho_0}{\varepsilon_r \varepsilon_0}, \tag{2.61}$$

where we used our sign convention from section 2.2 that $\vec{\mathcal{E}} = -\mathcal{E}\hat{x}$. The figure 2.9 illustrates the detector and the internal electric field.

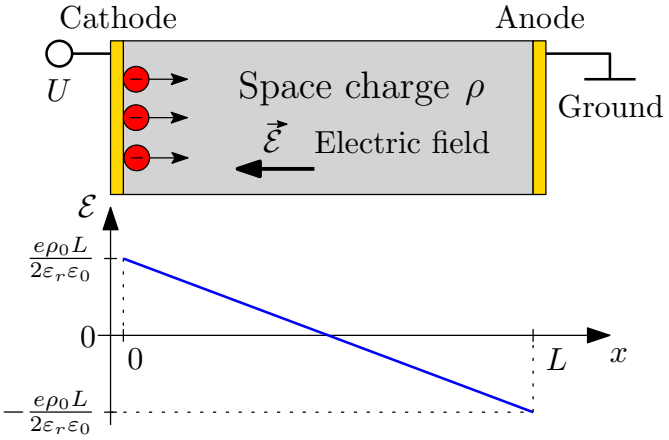

Figure 2.9: Scheme of the detector with constant space charge density and the electric field profile in the detector (blue line).

The equation (2.61) can be rewritten into

$$\mathcal{E}(x) = \mathcal{E}_0 - \frac{e\rho_0}{\varepsilon_r\varepsilon_0}x = \mathcal{E}_0 - ax, \tag{2.62}$$

where $\mathcal{E}_0$ is the electric field at $x = 0$ and a is the slope of the electric field

$$a = \frac{e\rho_0}{\varepsilon_r\varepsilon_0}. \tag{2.63}$$

The electric field field satisfies

$$U = \int_0^L \mathcal{E}(x)\mathrm{d}x. \tag{2.64}$$

Initial constant space charge in the detector cannot be sustained without applied bias ($U = 0$) at equilibrium and is neutralized [13]. If $U > 0$, the space charge can be sustained at equilibrium, but wherever the electric field before equilibrium is less than zero (the space charge screens out the bias completely), the inactive layer is formed. Inactive layer is a region inside the detector where the electric field is almost zero (small value of electric field is required from the continuity equation). The space charge in the inactive layer is quickly compensated by the free charge and at equilibrium the space charge disappears from this region [9]. The equation (2.62) has to be changed into equation

$$\mathcal{E}(x) = \max(\mathcal{E}_0 - ax, 0), \tag{2.65}$$

which is valid even in presence of the inactive layer [18]. From (2.64) the value of $\mathcal{E}_0$ can be found, which is dependent on the value of a for given bias U. Let's analyze the limit case when $\mathcal{E}(L) = 0$ and nonzero for $0 \leq x < L$ for given bias U [19]. From (2.65) this happens when $\mathcal{E}_0 - a_M L = 0$. Using equation (2.64) we get

$$a_M = \frac{2U}{L^2}, \tag{2.66}$$

where a_M is the slope of the electric field for which the inactive layer starts to form. For $a > a_M$ inactive layer is formed and for $-a_M < a < a_M$ there is nonzero electric field in whole detector and no inactive layer exist inside the detector. For $a < -a_M$ the inactive layer is under cathode. The position of inactive layer and active region boundary W can be found from relation for bias U (2.64) to be

$$W = \begin{cases} \min(\sqrt{\frac{2U}{|a|}}, L) & a > 0 \\ \max(L - \sqrt{\frac{2U}{|a|}}, 0) & a < 0, \end{cases} \tag{2.67}$$

from which the width of the inactive layer is $L - W$ for $a > 0$ and W for $a < 0$. The a_M and W are very important in the electric field analysis, which is shown in the figure 2.10, where red curve represent the case when $a = 0$ and detector has no space charge, green curve represents the case when $a = a_M = 2U/L^2$ and inactive layer starts forming at $W = L$. For $a > a_M$ inactive layer appears $W < L$ (orange curve). For $-a_M < a < 0$ the electric field is increasing (purple and cyan curves). For $0 < a < a_M$ the electric field is decreasing (orange, green and blue curves). For $a < -a_M$ inactive layer appears under cathode and no electrons can move though the detector since the inactive layer prevents it at $x = 0$ (purple curve).

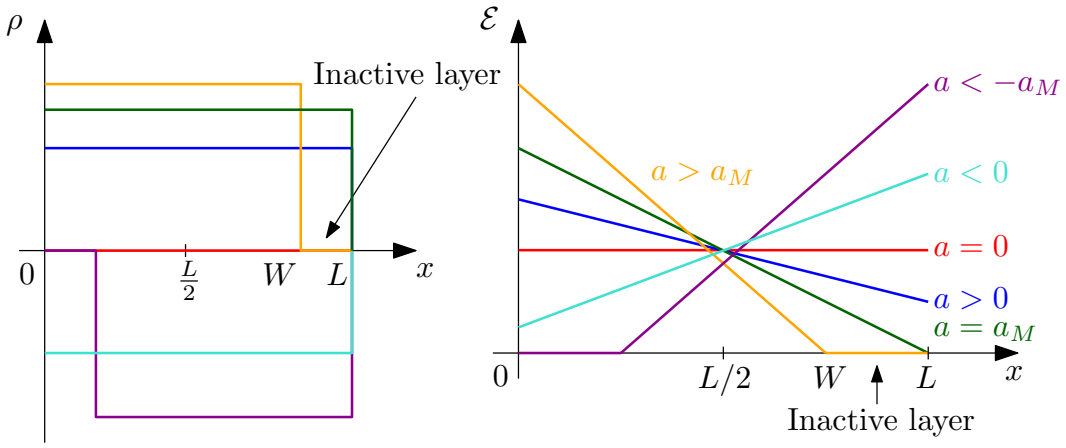

Figure 2.10: **Left**: Space charge densities for different values of a and the same bias U. **Right**: Electric field profiles.

The current waveform will be derived in a similar way to [20]. The general kinetic differential equation for electron position as a function of time is

$$v(t) = \frac{\mathrm{d}x}{\mathrm{d}t} = \dot{x}(t) = \mu_e \mathcal{E}(x(t)). \tag{2.68}$$

For linear electric field (2.65) for $|a| < a_M$. The equation (2.68) has form

$$\dot{x}(t) = \mu_e(\mathcal{E}_0 - ax), \tag{2.69}$$

and has solution

$$x(t) = C\exp\left(-\mu_e a t\right) + \frac{\mathcal{E}_0}{a}, \tag{2.70}$$

where C is determined from boundary condition $x(0) = 0$ from which $C = -\mathcal{E}_0/a$ and position $x(t)$ is

$$x(t) = \frac{\mathcal{E}_0}{a}\left(1 - \exp\left(-a\mu_e t\right)\right). \tag{2.71}$$

We assume here that the electron cloud arrives to the anode and is collected at transit time t_r . This is equivalent to $x(t_r) = L$ and from (2.71) using the relation (2.64) for bias $U = \mathcal{E}_0 L - aL^2/2$ and definition of a_M (2.66) the transit time t_r is

$$t_r = \frac{1}{a\mu_e}\ln\left(\frac{\mathcal{E}_0}{\mathcal{E}_0 - aL}\right) = \frac{1}{a\mu_e}\ln\left(\frac{1 + \frac{aL^2}{2U}}{1 - \frac{aL^2}{2U}}\right) = \frac{1}{a\mu_e}\ln\left(\frac{1 + \frac{a}{a_M}}{1 - \frac{a}{a_M}}\right), \tag{2.72}$$

where $a_M = \frac{2U}{L^2}$ is the maximum slope for which there is no inactive layer in the detector. From the last term in (2.72) it is evident that the transit time is finite for $-a_M < a < a_M$, infinite for $a = a_M$, and is not well defined for $a > a_M$ since the electron cloud never arrives to the anode because of the inactive layer. For $-a_M \leq a$ the inactive layer is under the cathode ($x = 0$) and the electron cloud doesn't move at all so the definition of the transit time has no sense. Transit time $t_r > T_R$ for $a \neq 0$ and for $a \to 0$ $t_r \to T_R = \frac{L}{\mu_e \mathcal{E}_0}$, which is the default transit time for the case with the constant electric field. From the knowledge of

$x(t)$, $v(t) = \dot{x}(t)$, t_r and $Q(t) = Q_0$ (no trapping) we can use the Shockley-Ramo theorem (2.8) to find the current waveform

$$I(t) = \frac{Q(t)v(t)}{L} = \frac{Q_0 \mathcal{E}_0 \mu_e}{L} \exp\left(-a\mu_e t\right) \chi_{[0,t_r]}(t). \tag{2.73}$$

This equation is also valid for $a > a_M$ with $t_r = +\infty$. To include one deep trap, Q_0 has to be replaced with $Q(t) = Q_0 \exp\left(-t/\tau_{TD}\right)$ in Shockley-Ramo theorem. This leads to the current waveform in the final form

$$I(t) = \frac{Q(t)\dot{x}(t)}{L} = \frac{Q_0 \mathcal{E}_0 \mu_e}{L} \exp\left(-(a\mu_e + \frac{1}{\tau_{TD}})t\right) \chi_{[0,t_r]}(t). \tag{2.74}$$

Analysis of current waveforms depending on transit time is shown in the figure 2.11, where the green curve represents the case when $a = a_M$ and the inactive layer starts forming at $W = L$. For $-a_M < a < 0$ the electric field is increasing (orange curve) and transit time $t_r > T_R$. For $0 < a < a_M$ the electric field is decreasing (blue curve) and $t_r > T_R$. For $a = 0$ no space charge exist inside the detector and $t_r = T_R$ (red curve).

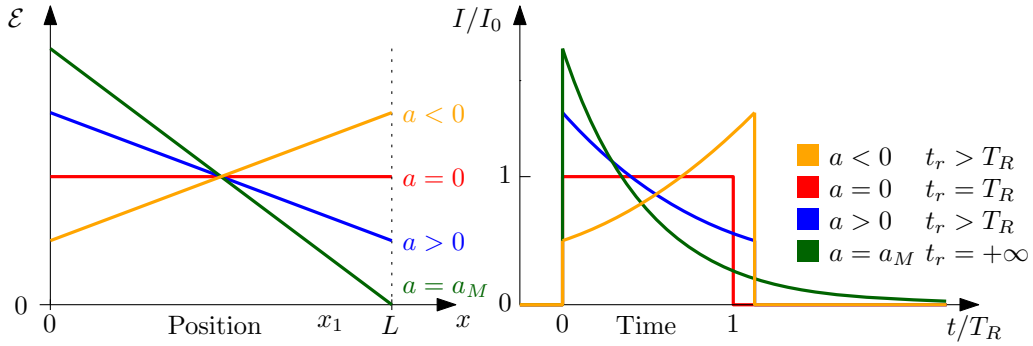

Figure 2.11: **Left**: Electric field for different values of a. **Right**: Normalized current waveforms.

2.7.2 Linear space charge profile

Let's assume a detector with linear profile of space charge density in the whole volume, which corresponds to the electric field with variable slope $a(x)$

$$\mathcal{E}(x) = \mathcal{E}_0 - a(x)x, \tag{2.75}$$

where

$$a(x) = \frac{\mathcal{E}_0 - \mathcal{E}_L}{L^2}x, \tag{2.76}$$

where $\mathcal{E}_0 = \mathcal{E}(0), \mathcal{E}_L = \mathcal{E}(L)$. This gives us parabolic electric field

$$\mathcal{E}(x) = \mathcal{E}_0 - \frac{\mathcal{E}_0 - \mathcal{E}_L}{L^2}x^2. \tag{2.77}$$

Space charge density ρ is found from (2.77) using differential form of the Gauss law, which is in our sign convention (see assumptions 2.2)

$$\rho(x) = -\frac{\varepsilon_r \varepsilon_0}{e}\frac{\mathrm{d}\mathcal{E}(x)}{\mathrm{d}x} = \frac{2\varepsilon_r \varepsilon_0}{e}\frac{\mathcal{E}_0 - \mathcal{E}_L}{L^2}x. \tag{2.78}$$

Current waveform will be found in similar way to the case with constant space charge in section 2.7.1 by solving the kinetic equation for electron cloud movement

$$\dot{x}(t) = \mu_e \left[\mathcal{E}_0 - \frac{\mathcal{E}_0 - \mathcal{E}_L}{L^2} x(t)^2 \right]. \tag{2.79}$$

This differential equation has analytic solution

$$x(t) = L\sqrt{\frac{\mathcal{E}_0}{\mathcal{E}_0 - \mathcal{E}_L}} \tanh\left(\frac{\mu_e}{L} \sqrt{\mathcal{E}_0(\mathcal{E}_0 - \mathcal{E}_L)}\ t \right). \tag{2.80}$$

From (2.80) using identity for hyperbolic tangent

$$\frac{\mathrm{d}\tanh(t)}{\mathrm{d}t} = 1 - \tanh^2(t) = \frac{1}{\cosh^2(t)}, \tag{2.81}$$

we get

$$\dot{x}(t) = \mu_e \mathcal{E}_0 \frac{1}{\cosh^2\left(\frac{\mu_e}{L} \sqrt{\mathcal{E}_0(\mathcal{E}_0 - \mathcal{E}_L)}\ t \right)}. \tag{2.82}$$

From (2.82) we directly get current waveform using the Shockley-Ramo theorem (2.8)

$$I(t) = \frac{Q_0 \mathcal{E}_0 \mu_e}{L} \frac{1}{\cosh^2\left(\frac{\mu_e}{L} \sqrt{\mathcal{E}_0(\mathcal{E}_0 - \mathcal{E}_L)}\ t \right)} \chi_{[0,t_r]}(t), \tag{2.83}$$

where transit time t_r is found from $x(t_r) = L$. Normalized current waveforms, space charge density and electric field are shown in figure 2.12, where red curve corresponds to case when no space charge is present inside the detector $\mathcal{E}_L = \mathcal{E}_0$ and $t_r = T_R$. Blue curve corresponds to intermediate space charge $\mathcal{E}_L \approx \mathcal{E}_0/2$ and $t_r > T_R$. Green curve corresponds to the limit case when $\mathcal{E}_L \approx 0$ and $t_r = +\infty$. One deep trap can be included into (2.83) by replacing Q_0 with $Q_0 \exp(-t/\tau_{TD})$.

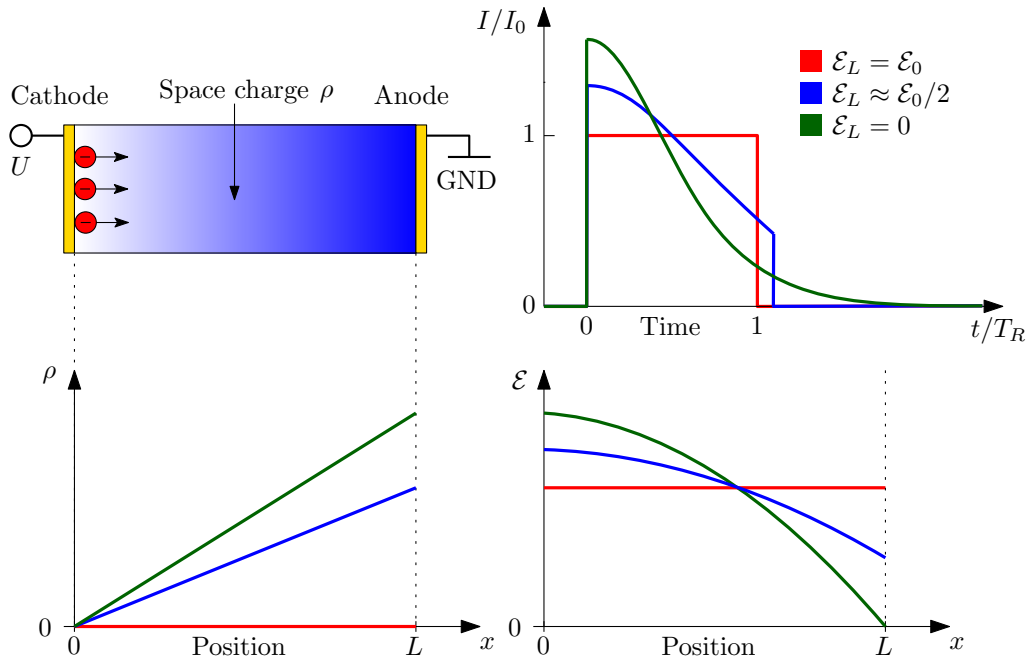

Figure 2.12: **Left top**: Scheme of the detector with linear profile of space charge. **Right top**: Current waveforms. **Left bottom**: Space charge density. **Right bottom**: Internal electric field.

2.7.3 Region of constant space charge

If the space charge is not constant inside the detector the analysis is more complicated. Let's assume that we have a detector with region with no space charge in interval $x \in [0, x_1]$ and constant space charge density for $x \in [x_1, L]$. The current waveform is comprised of two part corresponding to two regions in the detector. First is drift in constant electric field and and has form

$$I_1(t) = \frac{Q_0 \mathcal{E}_0 \mu_e}{L} \chi_{[0,T_{R1}]}(t), \tag{2.84}$$

where $T_{R1} = x_1/\mu_e \mathcal{E}_0$ is the transit time for the first region with constant electric field. The second component corresponds to the electron cloud movement through the region with constant space charge, which was discussed in subsection 2.7.1 and from (2.73) the contribution to current is

$$I_2(t) = \frac{Q_0 \mathcal{E}_0 \mu_e}{L} \exp\left(-a\mu_e(t - T_{R1})\right) \chi_{[0,t_{r2}]}(t - T_{R1}), \tag{2.85}$$

where t_{r2} is the transit time for the second region found from (2.72), where L is replaced with $L - x_1$ and $a = \frac{\mathcal{E}_0 - \mathcal{E}_L}{L - x_1}$. Transit time for both regions is $t_r = T_{R1} + t_{r2}$. When we combine both contributions (2.84) and (2.85) we get the total current

$$I(t) = \frac{Q_0 \mathcal{E}_0 \mu_e}{L} \left[\chi_{[0,T_{R1}]}(t) + \exp\left(-a\mu_e(t - T_{R1})\right) \chi_{[0,t_{r2}]}(t - T_{R1})\right]. \tag{2.86}$$

Normalized current waveforms, space charge density and electric field are shown in figure 2.13, where red curve corresponds to case when no space charge is present inside the detector $\mathcal{E}_L = \mathcal{E}_0$ and $t_r = T_R$. Blue curve corresponds to intermediate

space charge $\mathcal{E}_L \approx \mathcal{E}_0/2$ and $t_r > T_R$. Green curve corresponds to the limit case when $\mathcal{E}_L \approx 0$ and $t_r = +\infty$. Electric field $\mathcal{E}(x)$ is constant for $x \in [0, x_1]$ and linear function of position for $x \in [x_1, L]$.

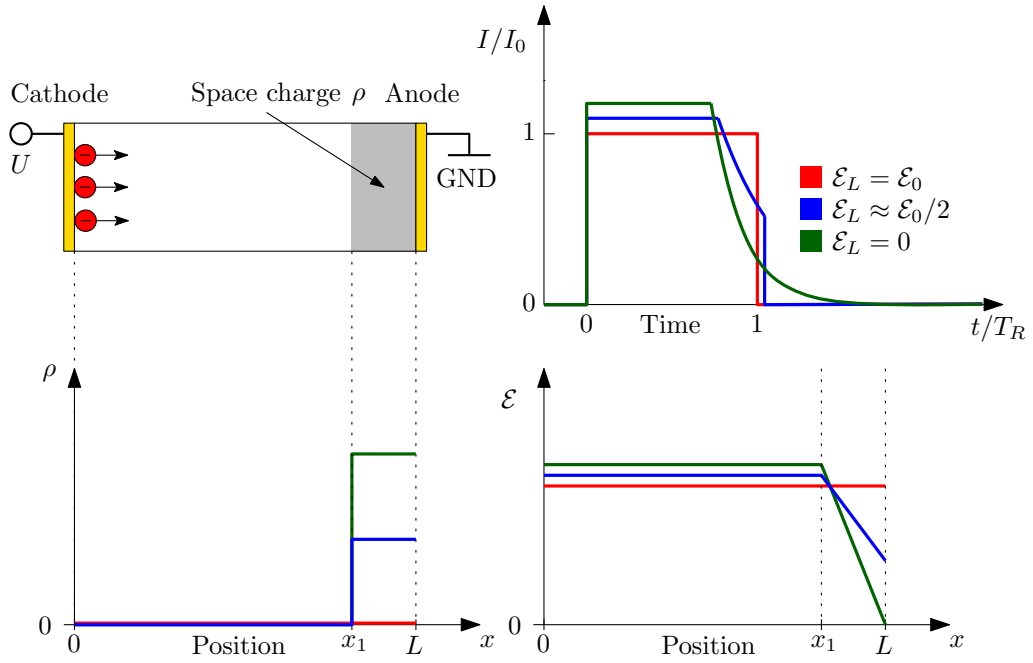

Figure 2.13: **Left top**: Scheme of the detector with constant space charge density ρ in region $x \in [x_1, L]$. **Right top**: Normalized current waveforms. **Left bottom**: Space charge density. **Right bottom**: Internal electric field.

2.7.4 Region of linear space charge

Let's assume a detector with the region with no space charge in the interval $x \in [0, x_1]$ and linear space charge density for $x \in [x_1, L]$. The current waveform comprises of two components corresponding to two regions in the detector, the analysis is similar to subsection 2.7.3. The first component represents drift of electrons in constant electric field and has form

$$I_1(t) = \frac{Q_0 \mathcal{E}_0 \mu_e}{L} \chi_{[0,T_{R1}]}(t), \tag{2.87}$$

where the $T_{R1} = x_1/\mu_e \mathcal{E}_0$ is the transit time for the first region with constant electric field. The second component corresponds to te electron cloud movement through the region with linear space charge, which was discussed in subsection 2.7.2 and the contribution to current is equal to (2.83), where we replace L in cosh with length of space charge region $L - x_1$

$$I_2(t) = \frac{Q_0 \mathcal{E}_0 \mu_e}{L} \frac{1}{\cosh^2\left(\frac{\mu_e}{L-x_1}\sqrt{\mathcal{E}_0(\mathcal{E}_0 - \mathcal{E}_L)}\ (t - T_{R1})\right)} \chi_{[0,t_{r2}]}(t - T_{R1}), \tag{2.88}$$

where t_{r2} is the transit time for the second region found from (2.80) using $x(t_{r2}) = L - x_1$. Transit time for both regions is $t_r = T_{R1} + t_{r2}$. When we combine both contributions (2.87) and (2.88) we get the total current

$$I(t) = I_1(t) + I_2(t). \tag{2.89}$$

Normalized current waveforms, space charge density and electric field are shown in figure 2.14, where red curve corresponds to case when no space charge is present inside the detector $\mathcal{E}_L = \mathcal{E}_0$ and $t_r = T_R$. Blue curve corresponds to intermediate space charge $\mathcal{E}_L \approx \mathcal{E}_0/2$ and $t_r > T_R$. Green curve corresponds to the limit case when $\mathcal{E}_L \approx 0$ and $t_r = +\infty$. Electric field $\mathcal{E}(x)$ is constant for $x \in [0, x_1]$ and parabolic function of position for $x \in [x_1, L]$.

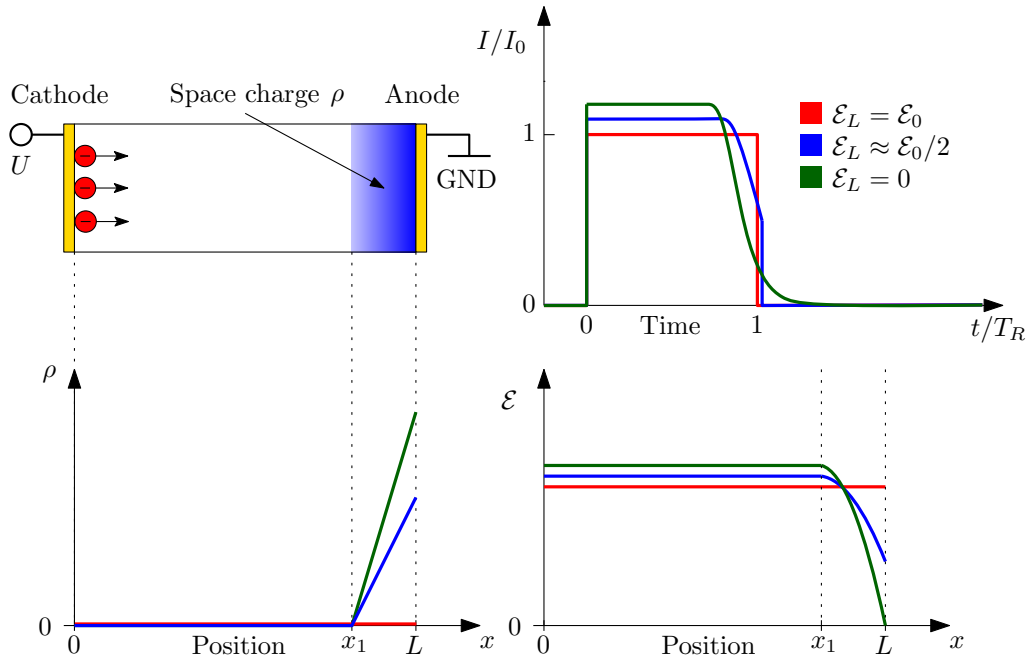

Figure 2.14: **Left top**: Scheme of the detector with linear space charge density ρ in region $x \in [x_1, L]$. **Right top**: Normalized current waveforms. **Left bottom**: Space charge density. **Right bottom**: Internal electric field.

2.7.5 Space charge limited current

Square root dependence of the internal electric field naturally arises in case of Space Charge Limited Currents (SCLC) [21]. This will be later shown in experimental section. Formula for electric field can be expressed in form

$$\mathcal{E}(x) = \sqrt{\mathcal{E}_0^2 + b^2 \frac{x}{L}}, \tag{2.90}$$

where $\mathcal{E}_0$ is the electric field under cathode, L is the detector thickness and b is parameter with dimension of electric field intensity that defines the steepness of square root. Space charge density ρ is

$$\rho(x) = -\frac{\varepsilon_r \varepsilon_0}{e} \frac{\mathrm{d}\mathcal{E}(x)}{\mathrm{d}x} = -\frac{\varepsilon_r \varepsilon_0 b^2}{2eL} \frac{1}{\sqrt{\mathcal{E}_0^2 + b^2 \frac{x}{L}}}. \tag{2.91}$$

Using kinetic equation for electron

$$\dot{x}(t) = \mu_e \mathcal{E}(x(t)) = \mu_e \sqrt{\mathcal{E}_0^2 + b^2 \frac{x(t)}{L}}. \tag{2.92}$$

This differential equation has solution:

$$x(t) = \frac{\mu_e^2 b^2}{4L}(t + C)^2 - \mathcal{E}_0^2 \frac{L}{b^2}, \tag{2.93}$$

where C is determined from boundary condition $x(0) = 0$ from which

$$C = \frac{2L\mathcal{E}_0}{\mu_e b^2} \tag{2.94}$$

and position $x(t)$ is

$$x(t) = \frac{\mu_e^2 b^2}{4L}\left(t + \frac{2L\mathcal{E}_0}{\mu_e b^2}\right)^2 - \mathcal{E}_0^2 \frac{L}{b^2}. \tag{2.95}$$

The other condition for $x(t)$ is that for transit time t_r the electron cloud arrives to the anode and is collected. This is equivalent to $x(t_r) = L$. From (2.95) we get

$$t_r = \frac{2L\mathcal{E}_0}{\mu_e b^2}\left(\sqrt{\frac{b^2}{\mathcal{E}_0^2} + 1} - 1\right). \tag{2.96}$$

This expression is well defined since it is always nonnegative and for $b \to 0$ $t_r \to T_R$, which is expected since the electric field (2.90) is constant $\mathcal{E}(x) = \mathcal{E}_0$ and for this case the transit time t_r is equal to the default transit time T_R (2.13). From the knowledge of $x(t), v(t) = \dot{x}(t)$, t_r and assuming no trapping $Q(t) = Q_0$ we can use the Shockley-Ramo theorem (2.8) to find the current waveform

$$I(t) = \frac{Q(t)v(t)}{L} = \left(\frac{Q_0\mu_e\mathcal{E}_0}{L} + \frac{Q_0\mu_e^2 b^2}{2L^2}t\right)\chi_{[0,t_r]}(t). \tag{2.97}$$

The current waveform is linear function of time bounded by the boxcar function, which is necessary to mark the transit time. Normalized current waveforms, space charge density and electric field are shown in figure 2.15, where red curve corresponds to case when no space charge is present inside the detector $\mathcal{E}_0 = \mathcal{E}_L$ and $t_r = T_R$. Blue curve corresponds to intermediate space charge $\mathcal{E}_0 \approx \mathcal{E}_L/2$ and $t_r > T_R$. Green curve corresponds to the limit case when $\mathcal{E}_0 \approx 0$ and $t_r > T_R$. The space charge density in (2.91) grows beyond any bound at $x = 0$ for $\mathcal{E}_0 \to 0$.

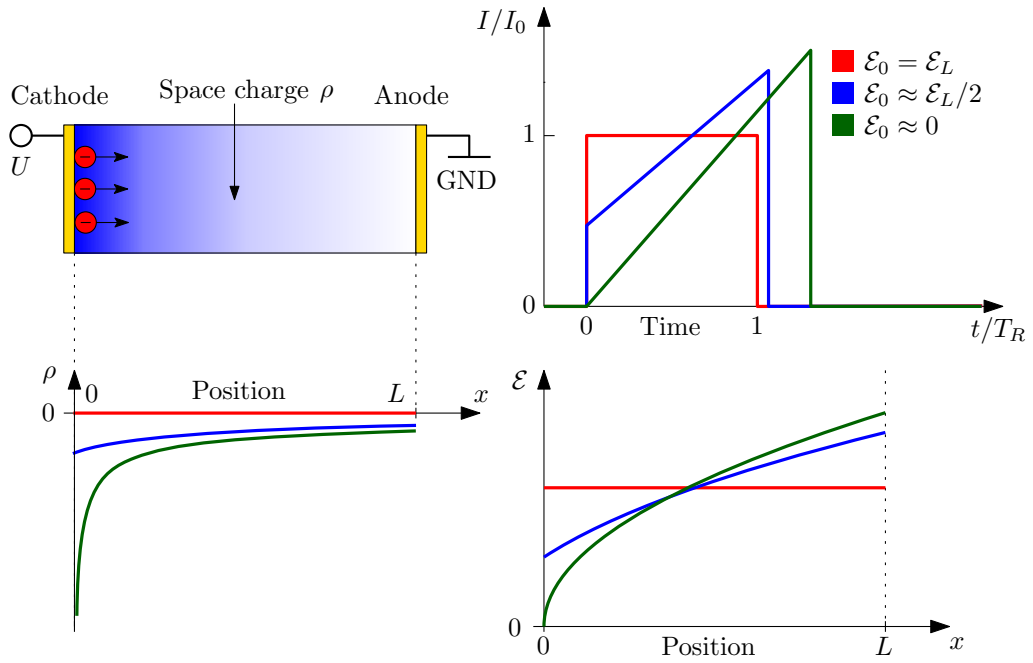

Figure 2.15: **Left top**: Scheme of the detector with space charge limit current. **Right top**: Normalized current waveforms. **Left bottom**: Space charge density. **Right bottom**: Internal electric field.

2.8 General space charge profile

The spatial dependence of the electric field intensity can be obtained from current waveforms for the detector with general space charge profile and one deep trap using the Shockley-Ramo theorem (2.8) and kinetic equation for electron (2.68), from which

$$x(t) = L \int_0^t \frac{i(t')}{Q(t')} \mathrm{d}t'. \tag{2.98}$$

Using equation for charge trapping (2.58) we get

$$x(t) = \frac{L}{Q_0} \int_0^t i(t') \exp\left(\frac{t'}{\tau_{TD}}\right) \mathrm{d}t'. \tag{2.99}$$

Electric field is from (2.8) and (2.58)

$$\mathcal{E}(t) = \frac{L}{\mu_e} \frac{I(t)}{Q(t)} = \frac{L}{\mu_e} \frac{I(t)}{Q_0} \exp\left(\frac{t}{\tau_{TD}}\right), \tag{2.100}$$

and the spatial dependence of electric field $\mathcal{E}(x)$ can be obtained from (2.99) and (2.100). This method works if diffusion and detrapping processes are negligible [22], however from our experiments diffusion and detrapping need to be included for correct evaluation of electric field inside the detector using Monte Carlo simulations.

2.9 Surface recombination

Surface recombination (SR) can be modeled by dividing the detector into a thin surface layer with thickness $x_S \ll L$ and the rest, which is treated as the bulk layer (see figure 2.16). The SR is characterized by the surface recombination velocity s, which defines the probability p_{bulk} of charge carrier entering from surface layer into the bulk [23]

$$\frac{p_{bulk}}{1-p_{bulk}} = \frac{v}{s}, \tag{2.101}$$

where v is the charge carrier drift velocity in the surface layer. From (2.101) we get

$$p_{bulk} = \frac{v}{v+s}. \tag{2.102}$$

The initially photogenerated charge Q_{00} in the surface layer will be partially recombined. Rest of the charge entering the bulk Q_0 is

$$Q_0 = Q_{00}\frac{v}{v+s}. \tag{2.103}$$

Surface recombination defined in this way only affects the photogenerated charge and thus only amplitude of measured current waveform is decreased. If there is constant internal electric field $\mathcal{E}(x) = \mathcal{E}_0$ in the detector, the drift velocity v is also constant $v = \mu_e\mathcal{E}_0 = \mu_e U/L$. This leads to the dependence of the initial charge Q_0 on bias U

$$Q_0 = Q_{00}\frac{1}{1+\frac{sL}{\mu_e U}}. \tag{2.104}$$

This equation shows the saturation of initial charge Q_0 to the value Q_{00} as the bias U increases. The current waveform for the detector with one deep trap (see subsection 2.6.2) is

$$I(t) = \frac{Q_0\mu_e U}{L^2}\exp\left(-\frac{t}{\tau_{TD}}\right)\chi_{[0,T_R]}(t). \tag{2.105}$$

In case of SR the Q_0 is replaced from (2.104). One method to recognize if the surface recombination is present in the detector is to normalize each current waveform by its bias. From (2.105) it is evident that after normalization, the amplitude of current waveforms is bias independent in case of no SR and in case with SR there is bias dependence of current waveform amplitude. Current waveforms normalized by respective bias for detector without SR lie on each other in overlapping intervals while for detector with SR current waveform have different values. This can be used to recognize presence of SR in experiments. The bias normalization of current waveforms is shown in figure 2.17, where current waveform in case with SR has lower amplitude for given bias than in case without SR (see dotted lines).

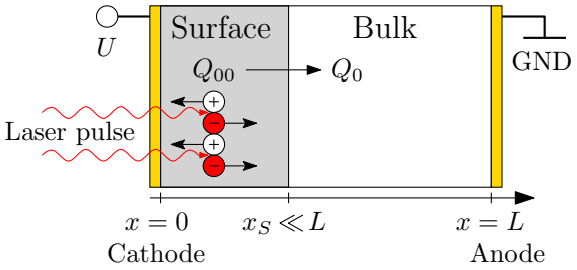

Figure 2.16: Detector with surface layer and bulk. Initially photogenerated charge Q_{00} is partially recombined and only part Q_0 enters the bulk.

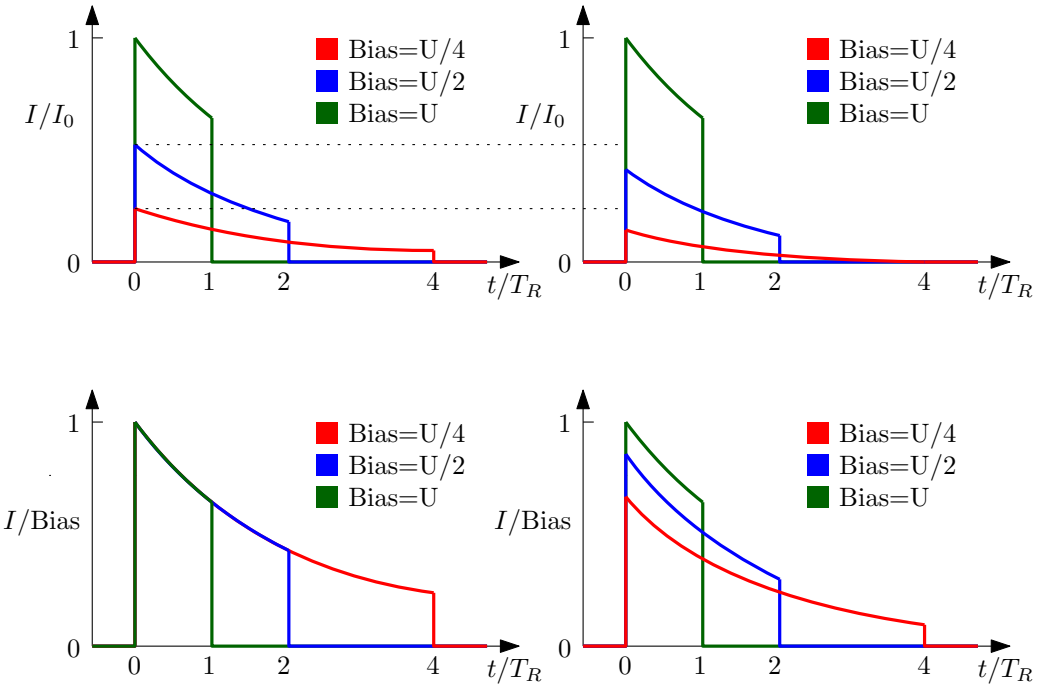

Figure 2.17: **Left Top**: Normalized current waveforms for the detector without surface recombination (SR). **Right Top**: Normalized current waveforms for the detector with SR. **Left bottom**: Current waveforms normalized by respective bias for detector without SR. **Right bottom**: Current waveforms normalized by respective bias for detector with SR.

3. Monte Carlo Simulation

3.1 Concept of Monte Carlo simulation

Theoretical calculation of current waveform based on current continuity equations is rather complicated and analytical solution for time beyond T_R exist only if one trap level is present in the detector [10]. Other possibility to calculate current waveform is to use a numerical method based on one dimensional Monte Carlo (MC) simulation of the motion of photogenerated charge carriers under applied electric field that is perpendicular to planar electrodes. Monte Carlo simulations are widely used for carrier transport study [13]. In [24] comprehensive review of MC simulation with detailed microscopic scattering mechanisms is shown. We use simpler MC simulation based on more phenomenological concept shown in [10]. The goal is to expand mentioned concept to include arbitrary internal electric field profile, effects of diffusion, wavelength of excitation laser pulse and other parameters. Our concept of MC simulation based on [10] is shown in figure 3.1, where each line represents time evolution of one carrier. Filled circles indicate carriers in the free state and open circles indicate carriers that are trapped. At each time step Δt carriers drift toward the collecting electrode by distance $\Delta x = v(x)\Delta t$ or remain trapped. The excess photogenerated carriers in the detector are represented by $\mathcal{N}$ "superparticles" where each superparticle represents several thousands real carriers (electrons or holes).

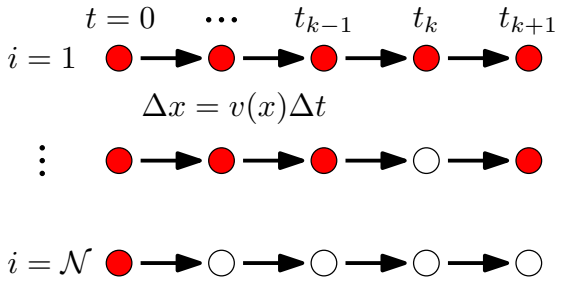

Figure 3.1: Basic concept of Monte Carlo simulation.

The total amount of photogenerated charge in the detector is Q_0, which gives the charge of a superparticle

$$q = \frac{Q_0}{\mathcal{N}}. \tag{3.1}$$

We assume that these superparticles are not interacting with each other. The detector is rectangular with two planar electrodes on opposite sides. Distance between electrodes (detector thickness) is L. The detector is held under constant bias U with electric field profile (intensity of electric field) $\mathcal{E}(x)$, which can be an arbitrary function of position and is independent on time during simulation. Position x is oriented from the cathode ($x = 0$) to the anode ($x = L$). The described geometry is the same as the one used in assumptions (see figure 2.1 in chapter 2).

3.2 Initial distribution of carriers

At the beginning of the simulation ($t = 0$) the incoming laser pulse generates all carriers with positions according to the Lambert-Beer absorption law for light (2.17). Since we are generating exactly $\mathcal{N}$ superparticles inside the detector $[0, L]$, the probability distribution of initial positions of carriers $\mathcal{P}(x)$ is then

$$\mathcal{P}(x) = \frac{\alpha \exp(-\alpha x)}{1 - \exp(-\alpha L)} \chi_{[0,L]}(x), \tag{3.2}$$

which is renormalized Lambert-Beer law (2.17), where α is the absorption coefficient and $\chi_{[0,L]}(x)$ assures that $\mathcal{P}(x)$ is zero outside the detector where are no generated carriers (this speeds up the random number generation of carrier by eliminating tries outside the detector for small values of α). $\mathcal{P}(x)$ holds the norm for probability distribution

$$\int_0^{+\infty} \mathcal{P}(x)\mathrm{d}x = 1. \tag{3.3}$$

Figure 3.2 illustrates the scheme of the detector with photogenerated electron-hole (e-h) pairs according to the Lambert-Beer law. The probability distribution (3.2) is randomly sampled giving initial position for each carrier (details in section 3.5).

If the light is strongly absorbed ($\alpha \cdot L \gg 1$), all carriers are generated near under the cathode, one type of carriers is immediately collected and the other type of carriers drifts through the bulk.

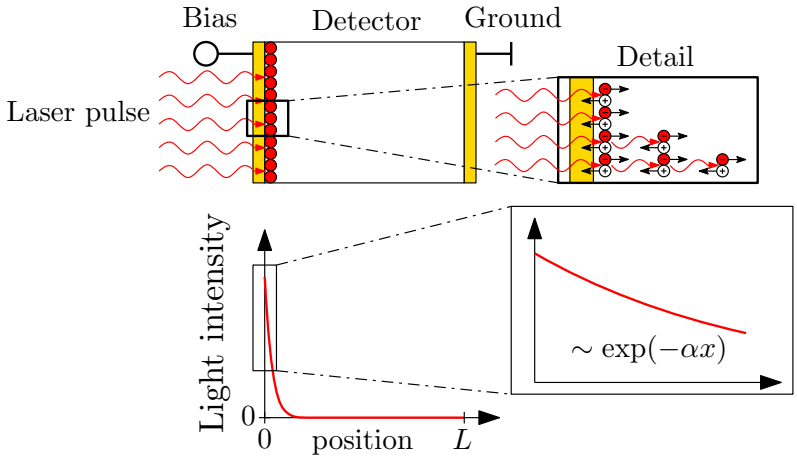

Figure 3.2: **Top**: Scheme of the detector with incident laser pulse generating e-h pairs according to the Lambert-Beer law. Photogenerated electron-hole pairs are separated by the electric field. Electrons drift into the bulk towards the anode and holes drift to the cathode. **Bottom**: Intensity of light as a function of position.

The initial time distribution of carriers is given by laser pulse duration and shape. This distribution can be thought of in context of MC simulation as an arbitrary function of time $\mathcal{P}(t)$ that holds norm for the time probability distribution

$$\int_0^{+\infty} \mathcal{P}(t)\mathrm{d}t = 1. \tag{3.4}$$

This states that a carrier will eventually be generated so there will be exactly $\mathcal{N}$ superparticles after the end of the laser pulse. Simple example of the initial time distribution of carriers is the boxcar function, which represents the square laser pulse

$$\mathcal{P}(t) = \frac{1}{t_l}\chi_{[0,t_l]}(t), \tag{3.5}$$

where t_l is the duration of laser pulse. This probability distribution is randomly sampled giving generation time for each carrier (details in section 3.5).

3.3 Carrier dynamics

At each calculation time step t_k, the status of each carrier is determined by a Monte Carlo technique based on repeated random sampling. Only three carrier dynamics are possible [10]. First is that a carrier is drifting in the conduction (valence) band toward the collecting electrode. Second possibility is that a carrier is being trapped in the J-th trap level and third is that a carrier is being detrapped from the K-th trap level. Direct transition between J-th and K-th trap level is not assumed. This procedure is repeated until required duration of simulation is reached.

3.3.1 Carrier drift

If the i-th carrier is free in time step t_k then it drifts in the conduction (valence) band toward the collecting electrode by distance

$$\Delta x_i = \mu\mathcal{E}(x_i)\Delta t + u, \tag{3.6}$$

where μ is the carrier mobility (μ_e for electrons and μ_h for holes), $\mathcal{E}(x_i)$ is the electric field at position of the i-th carrier x_i, Δt is the duration of simulation time step and u is a small random offset with Gaussian distribution $\mathcal{P}(u)$ simulating carrier diffusion

$$\mathcal{P}(u) = \frac{1}{\sqrt{4\pi D\Delta t}} \exp\left(-\frac{u^2}{4D\Delta t}\right), \tag{3.7}$$

where D is diffusion coefficient given by Einstein relation (2.3). This probability distribution corresponds to the shape of the carrier cloud that has spread due to diffusion for time Δt from initially $\delta(x)$ shape (see section 2.5). Repeatedly applied random offset u to every carrier at each time step results in carrier spreading that approximates diffusion. If $x_i + \Delta x_i \geq L$ or $x_i + \Delta x_i \leq 0$, carrier is collected on electrode and don't contribute to the simulation anymore. The electric field $\mathcal{E}(x)$ is an arbitrary function of position given by space charge inside the detector and holds

$$U = \int_0^L \mathcal{E}(x)\mathrm{d}x, \tag{3.8}$$

where U is the applied bias. Typically for constant space charge distribution in the detector, $\mathcal{E}(x)$ is a linear function of position

$$\mathcal{E}(x) = \max(\mathcal{E}_0 - ax, 0), \tag{3.9}$$

where $\mathcal{E}_0$ is the electric field under the irradiated cathode and a is the slope of the electric field (for details see section 2.7).

3.3.2 Carrier trapping and detrapping

Second carrier dynamics is that a carrier is being trapped in J-th trap level and third is that a carrier is being detrapped from the K-th trap level. Direct transition between J-th and K-th trap level is not assumed. The probability per unit time for a previously free carrier being trapped into J-th level is $1/\tau_{TJ}$ where τ_{TJ} is the trapping time of the J-th trap level [7]. The probability per unit time for a carrier in the K-th trap level being released is $1/\tau_{DK}$ where τ_{DK} is the detrapping time of the K-th trap level. The trapping time can be interpreted as a mean free time for which a carrier drifts in the conduction (valence) band before it is trapped and the detrapping time is a mean time that a carrier spends in a trap before it is released (see section 2.6). The total probability per unit time for a previously free carrier being trapped $1/\tau_T$ is equal to the sum of probabilities for each trap level

$$\frac{1}{\tau_T} = \sum_{J=1} \frac{1}{\tau_{TJ}}. \tag{3.10}$$

If a carrier is free at some point in time, the probability of its remaining free for additional time step Δt is

$$p_F(\Delta t) = \exp\left(-\frac{\Delta t}{\tau_T}\right), \tag{3.11}$$

which follows from the definition of τ_{TJ} resp. τ_T [7]. Using simulation time step $\Delta t \ll \tau_T$, we get from (3.11)

$$p_F(\Delta t) = 1 - \frac{\Delta t}{\tau_T}. \tag{3.12}$$

Probability of initially free carrier to be trapped p_T in time Δt is

$$p_T(\Delta t) = 1 - p_F(\Delta t) = \frac{\Delta t}{\tau_T}. \tag{3.13}$$

Using (3.10) and (3.13)

$$p_T(\Delta t) = \sum_{J=1} \frac{\Delta t}{\tau_{TJ}} = \sum_{J=1} p_{TJ}(\Delta t), \tag{3.14}$$

where

$$p_{TJ}(\Delta t) = \frac{\Delta t}{\tau_{TJ}} \tag{3.15}$$

is the probability of initially free carrier to be trapped into the J-th trap in time Δt. Analogically for a carrier trapped in the J-th trap level the probability of it being detrapped p_{DJ} in time Δt is

$$p_{DJ}(\Delta t) = \frac{\Delta t}{\tau_{DJ}}. \tag{3.16}$$

For the description of trapping and detrapping phenomena, two trap level model [10] with one shallow and one deep trap is usually used. In this work we also follow this model (see subsection 2.6.1), where the shallow trap is labeled with index $J = S$ and trapping (detrapping) time is τ_{TS}, τ_{DS}. The deep trap is labeled with index $J = D$ and trapping (detrapping) time is τ_{TD}, τ_{DD}. Equations (3.13) and (3.16) will be used in calculation of trapping and detrapping probabilities in time step Δt (more details in section 3.5).

3.4 Electric current

At each time step t_k the current $I(t_k)$ is calculated according to the Shockley-Ramo theorem (see section 2.3)

$$I(t_k) = \sum_{i=1}^{\mathcal{N}} \frac{q\Delta x_i}{L\Delta t}, \tag{3.17}$$

where Δx_i is the distance that i-th carrier drifts in the time step t_k and q is charge of a superparticle (see (3.1)). If a carrier is trapped then its $\Delta x_i = 0$ and this carrier doesn't contribute to the current.

3.5 Overview of algorithm

In this section a pseudo-code of the described MC simulation will be shown. For this purposes the i-th carrier (superparticle) is characterized by its position x_i and its state s_i. Carrier can be in one of the three possible states:

1. **Waiting for generation** - The carriers are generated in time according to probability distribution $\mathcal{P}(t)$ describing the duration and shape of the laser pulse (see (3.5)).
2. **Free** - drifting in conduction (valence) band
3. **Trapped** - trapped in the J-th trap level

The MC simulation pseudo-code is shown in Algorithm 1. The procedure SIMULATION starts with calling procedure INITIALIZATION where for each carrier the initial position x_i is randomly sampled from probability distribution $\mathcal{P}(x)$ from the Lambert-Beer law (3.2) using inverse transformation method [25]. From the duration and shape of the laser pulse the i-th carrier is generated in the k_i simulation step, which is randomly sampled from $\mathcal{P}(t)$ (3.5) using inverse transformation method. The simulation step k_i when the i-th carrier is generated can be though of as a waiting time, which is decreased by 1 in every time step until it is 0, then the carrier is generated and can drift or be trapped in J-th trap level. These informations can be conveniently recorded into the state of the i-th carrier s_i, which is summarized in

$$s_i = \begin{cases} k_i > 0 & \text{if a carrier is waiting } k_i \text{ steps before generation} \\ 0 & \text{if a carrier is in the free state} \\ -J < 0 & \text{if a carrier is trapped in } J\text{−th trap level.} \end{cases} \tag{3.18}$$

From the value of s_i the charge dynamics are decided in procedure STEP where first is checked whether the carrier is inside the detector and is not collected on electrode. After that if the carrier is waiting to be generated ($s_i > 0$), s_i is decreased by 1. If the carrier is free ($s_i = 0$), it is randomly decided whether it stays free or becomes trapped according to probabilities shown in figure 3.3, where trapping probabilities for two trap levels and the probability that the carrier remains free are represented by line segments. Random real number r is uniformly generated in the interval $[0, 1]$ (see procedure RANDOM) and the state s_i is assigned according to the line segment in which r lies (see procedure GETTRAP). If r lies in red segment, carrier is trapped in $J = 1$ trap level and $s_i = -1$. If r lies in blue segment, carrier is trapped in $J = 2$ trap level and $s_i = -2$. If r lies in green segment, carrier is free and $s_i = 0$.

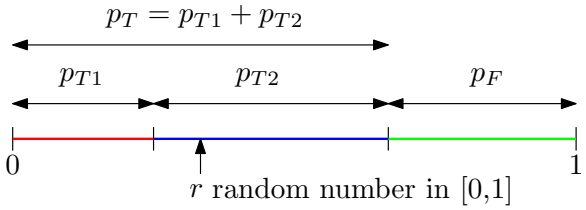

Figure 3.3: The line segments represent probabilities of carrier trapping into J-th trap level p_{TJ} and probability of being in the free state p_F. The total probability of trapping into any trap level is $p_T = p_{T1} + p_{T2}$ for two trap levels.

If the carrier becomes free, it drifts, this is done by calling procedure DRIFT, which updates the position x_i of the i-th carrier according to (3.6). If the carrier is trapped in J-th trap level ($s_i = -J < 0$), it is randomly decided whether the carrier stays trapped or becomes free according to the probability p_{DJ}.

This described carrier dynamics in procedure STEP is called for each carrier, after calculating carrier dynamics in simulation step the current is calculated from equation (3.17).

Algorithm 1 Monte Carlo

```
1: procedure SIMULATION
2:     INITIALIZATION()                          ▷ Initialize simulation
3:     for k ← 1, k_max do                       ▷ For each time step t_k
4:         for i ← 1, 𝒩 do                       ▷ Loop through all 𝒩 carriers
5:             STEP(i)                           ▷ Call time step procedure
6:         end for
7:         CALCCURRENT()                         ▷ Calculate current of all free carriers
8:     end for
9: end procedure
10: procedure INITIALIZATION
11:     for i ← 1, 𝒩 do                          ▷ Loop through all 𝒩 carriers
12:         x_i ← random sample of 𝒫(x)           ▷ see Lambert-Beer law (3.2)
13:         s_i ← random sample of 𝒫(t)           ▷ see Laser pulse shape (3.5)
14:     end for
15: end procedure
16: procedure STEP(i)                             ▷ Time step procedure of i-th carrier
17:     if x_i ∈ [0, L] then                      ▷ Check if carrier is not collected
18:         if s_i > 0 then                       ▷ Is carrier waiting before its generation?
19:             s_i ← s_i − 1                     ▷ decrease time steps s_i before generation
20:         else if s_i = 0 then                  ▷ Is carrier in free state?
21:             if RANDOM() < p_T then            ▷ Will be carrier trapped?
22:                 s_i = GETTRAP()               ▷ Set carrier into trapped state
23:             else
24:                 DRIFT()                       ▷ Carrier is now free and can drift
25:             end if
26:         else if s_i < 0 then                  ▷ Is carrier in trapped state?
27:             J ← −s_i                          ▷ get the index of trap level J from s_i
28:             if RANDOM() < p_DJ then           ▷ Will be carrier free?
29:                 s_i = 0                       ▷ Set carrier into free state
30:             end if
31:         end if
32:     end if
33: end procedure
34: procedure RANDOM
35:     Generates a random real number uniformly in [0, 1]
36: end procedure
37: procedure GETTRAP
38:     Randomly selects trap according to probability distribution described in
39:     section 3.5 and returns negative index of trap (-1 for the first trap level
40:     and so on).
41: end procedure
42: procedure DRIFT     ▷ Updates position of i-th carrier x_i by Δx from (3.6)
43:     x_i ← x_i + μ𝓔(x_i)Δt + u
44: end procedure
45: procedure CALCCURRENT
46:     Calculates current from equation (3.17)
47: end procedure
```

3.6 Visualization of the MC simulation

Visualization of the MC simulation is developed to see carrier trajectories, which helps us to understanding the connection between electric current and carrier cloud evolution. While it is possible to just show electric current as an output of the simulation, one would lose the information about carrier cloud shape. Since this MC simulation is 1D all carriers can move only on horizontal x-axis. For visualization we will offset each carrier in vertical y-axis to better see its trajectory. This will have no other purpose, vertical position of carrier has no effect on simulation what so ever. We will also use carrier concentration calculated from the distribution of carriers in space. The carrier concentration is normalized to see its details. Visualization of the MC simulation is shown in figure 3.4.

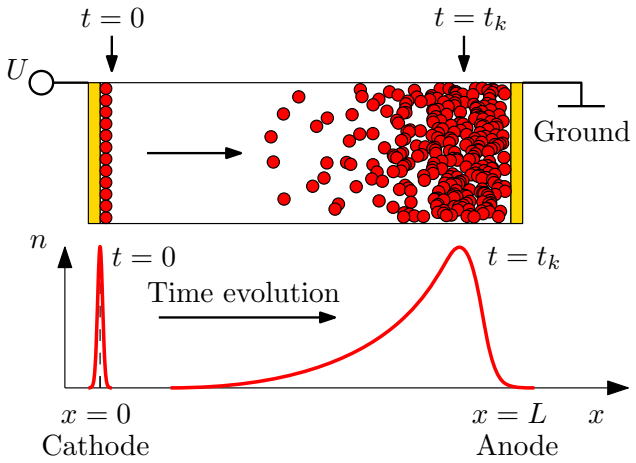

Figure 3.4: **Top**: Visualization of the carriers (red circles) in the detector at time $t = 0$ and $t = t_k$. Carriers can only move in horizontal direction (1D simulation). Vertical dimension is used only for carrier visualization. At $t = 0$ all carriers are generated under left electrode. At simulation step t_k the carrier cloud has evolved and moved to right. **Bottom**: Normalized carrier concentration at time $t = 0$ and $t = t_k$.

3.7 Shallow trap approximation beyond T_R

If there is only one shallow electron trap in the detector, analytical solution of current waveform for $0 < t < T_R$ can be found similarly to the case with two trap levels studied in section 2.6.1 by setting $\tau_{TD} \to +\infty$, from which $\tau_1 = +\infty$, $\tau_2 = \tau_e$, $A = \tau_e/\tau_{DS}$, $B = \tau_e/\tau_{TS}$. The current waveform (2.54) can be then rewritten in more convenient form

$$I(t) = \frac{Q_0}{T_R}\left[\frac{\tau_e}{\tau_{DS}} + \frac{\tau_e}{\tau_{TS}}\exp\left(-\frac{t}{\tau_e}\right)\right], \tag{3.19}$$

where τ_e is defined as

$$\frac{1}{\tau_e} = \frac{1}{\tau_{TS}} + \frac{1}{\tau_{DS}}. \tag{3.20}$$

Time τ_e is the mean time that in which the electron cloud thermalizes with the shallow trap. The current waveform (3.19) has two components. The first is the equilibrium term representing constant current. The second term represents filling of the shallow level that was initially empty. The current waveform (3.19) was shown in [16] where the detector with one trap level was studied. Analytical solution derived using probability calculations was shown in [7].

For $t > T_R$ due to the collection of electrons on the anode, the analytical current waveform (3.19) is not valid. We need to change (2.33) to

$$\frac{\mathrm{d}n}{\mathrm{d}t} = -\frac{n}{\tau_{TS}} + \frac{n_S}{\tau_{DS}} - \frac{n}{\tau_{TD}} - \mu\mathcal{E}_0\mathcal{A}n(L,t), \tag{3.21}$$

where $\mathcal{A}$ is the area of the anode, n is the concentration of electrons in the conduction band and $\mathcal{E}_0 = \frac{U}{L}$ is the constant electric field inside the detector. The last term in (3.21) represents the flux of electrons escaping the detector $n(L,t) = 0$ for $0 \leq t < T_R$ (no electrons are collected before T_R) and in this case no analytical solution exist for $t > T_R$ [16]. To find solution for $t > T_R$ numerical approach such as MC simulation has to be used or approximations have to be made, which were mentioned in [16]. Deeper analysis is needed to understand various effect of shallow trap. In the following two subsections two approximations of current waveforms for $t > T_R$ will be proposed, discussed in detail and compared with MC simulation.

3.7.1 Trap controlled mobility

Concept of trap controlled mobility was introduced in theoretical work [7] and in experimental works [26],[8]. Current waveforms with trap controlled mobility and trap controlled diffusions were not shown in cited papers, therefore current waveforms are discussed in detail in this subsection. Let's start with the Central limit theorem, which in our model states that when carriers undergo many trapping and detrapping events the overall shape of the electron cloud that was initially of an arbitrary shape will have the Gaussian function shape [27]. This allows us to make several simplifications and find the solution beyond the default transit time T_R. We shall assume that an electron spends on average time t_f in the free state moving with mobility μ_e and spends time t_{tr} in the trapped state not moving. Then we define the effective electron mobility μ_{eff}

$$\mu_{eff} = \mu_e \frac{t_f}{t_f + t_{tr}}, \tag{3.22}$$

which summarizes the fact that electron moves on average only for time t_f in total time interval $t_f + t_{tr}$, which effectively reduces its mobility μ_e to the effective mobility μ_{eff} by the ratio

$$\frac{t_f}{t_f + t_{tr}}. \tag{3.23}$$

The trapping time of shallow trap τ_{TS} can be interpreted as a mean time for which an electron is in free state and the detrapping time τ_{DS} is a mean time which an electron spends trapped. This leads to relation $t_f = \tau_{TS}$ and $t_{tr} = \tau_{DS}$ and when put in (3.22)

$$\mu_{eff} = \mu_e \frac{\tau_{TS}}{\tau_{TS} + \tau_{DS}}. \tag{3.24}$$

With this effective mobility we can define the effective transit time T'_R by replacing μ_e in (2.13) with μ_{eff}

$$T'_R = T_R \frac{\tau_{TS} + \tau_{DS}}{\tau_{TS}}. \tag{3.25}$$

During time t happen on average $\eta(t)$ trapping and detrapping events, which is

$$\eta(t) = \frac{t}{\tau_{TS} + \tau_{DS}}. \tag{3.26}$$

Average trapping/detrapping event chain is shown in the figure 3.5. Because of trapping and detrapping phenomena, electrons move on average more slowly and measured mobility and transit time no longer correspond to the microscopic electron mobility and default transit time but rather to their effective values. Central limit theorem gives us the value of the final variance of the Gaussian distribution σ_η^2 after η random events to be [27]

$$\sigma_\eta^2 = \eta\sigma^2, \tag{3.27}$$

if we know the elemental variance σ^2 of the underlying random process, which is in our case trap/detrap event and $\eta(t)$ is the number of trap/detrap events in the time t. The mean time that it takes electron cloud to thermalize with the shallow trap is τ_e (see its definition (3.20)), which is very important in the Central limit

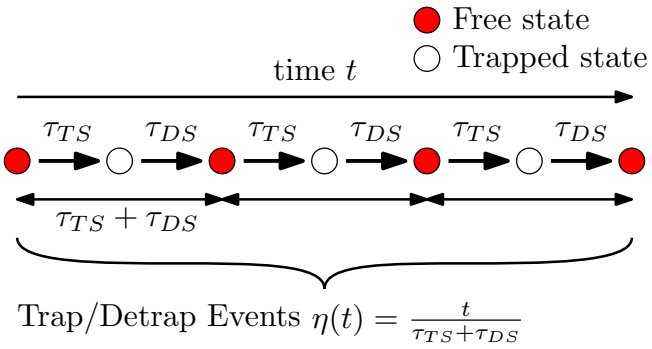

Figure 3.5: Illustration of the average trapping/detrapping event chain. Filled circle indicates an electron in the free state, open circle indicates an electron in the trapped state. During time t happen on average $\eta(t)$ trapping and detrapping events.

theorem because τ_e can be viewed as the standard deviation in the elemental process of trapping and detrapping in the time domain. This can be transformed to the spatial domain by relation $x = v_0 t$, where $v_0 = \mu_e \mathcal{E}_0 = L/T_R$, from which $\sigma^2 = v_0^2 \tau_e^2$. Since the Central limit theorem says that the final distribution $P_\eta(x,t)$ is Gaussian

$$P_\eta(x,t) = \frac{1}{\sqrt{2\pi\sigma_\eta^2}} \exp\left(-\frac{(x - v_{eff}t)^2}{2\sigma_\eta^2}\right) \tag{3.28}$$

where the centroid of the Gaussian electron cloud moves with the effective drift velocity $v_{eff} = \mu_{eff}\mathcal{E}_0$ and σ_η is the standard deviation

$$\sigma_\eta^2 = \eta\sigma^2 = \frac{v_0^2 \tau_e^2 t}{\tau_{TS} + \tau_{DS}}, \tag{3.29}$$

where η is from (3.26). The electron concentration $n(x,t)$ is found similarly to the discussion of the detector with diffusion in section 2.5

$$n(x,t) = \mathcal{N}_0\, \Theta(t) P_\eta(x,t) \chi_{[0,L]}(x) \tag{3.30}$$

By comparison of (3.30) using (3.29) with the equation for diffusion (2.27) we get the effective diffusion constant D_{eff}

$$D_{eff} = \frac{v_0^2 \tau_e^2}{\tau_{TS} + \tau_{DS}} = v_0^2 \frac{(\tau_{TS}\tau_{DS})^2}{(\tau_{TS} + \tau_{DS})^3}. \tag{3.31}$$

Effective diffusion constant D_{eff} is dependent on electric field through $v_0 = \mu_e \mathcal{E}_0$ and can be distinguished from ordinary diffusion coefficient D_e, which is given by the Einstein relation (2.3) and is independent on electric field. The electron concentration $n(x,t)$ is analogical to (2.27), where the diffusion constant D_e is replaced by D_{eff} and drift velocity v_0 is replaced by v_{eff}

$$n(x,t) = \mathcal{N}_0\, \Theta(t) \left(\frac{1}{4\pi D_{eff} t}\right)^{1/2} \exp\left(-\frac{(x - v_{eff}t)^2}{4D_{eff}t}\right) \chi_{[0,L]}(x). \tag{3.32}$$

Current waveform is similar to (2.30)

$$I(t) = \frac{Q_0}{T'_R}\,\Theta(t)\frac{1}{2}\left[\operatorname{erf}\left(\frac{L - v_{eff}t}{\sqrt{4D_{eff}t}}\right) + \operatorname{erf}\left(\frac{v_{eff}t}{\sqrt{4D_{eff}t}}\right)\right]. \tag{3.33}$$

The current waveform (3.33) is valid for $t \gg \tau_{TS} + \tau_{DS}$, from which $\eta \to +\infty$ and Central limit theorem is fulfilled. With (3.33) the analytical current waveform (3.19) can be extended beyond T_R into

$$I(t) = \frac{Q_0}{T_R}\,\Theta(t)\left[\frac{\tau_e}{\tau_{DS}} + \frac{\tau_e}{\tau_{TS}}\exp\left(-\frac{t}{\tau_e}\right)\right]\frac{1}{2}\left(\operatorname{erf}\left(\frac{L - v_{eff}t}{\sqrt{4D_{eff}t}}\right) + 1\right), \tag{3.34}$$

where we used for $t \to 0$ the analytical current waveform (3.19) and for $t \to T'_R$ we used the trap controlled mobility approximation (3.33) with

$$\lim_{t\to+\infty} \operatorname{erf}\left(\frac{v_{eff}t}{\sqrt{4D_{eff}t}}\right) = 1. \tag{3.35}$$

Current waveform (3.34) was tested using MC simulation. In figure 3.6, there is shown an example of carrier cloud evolution for $\tau_{TS}/T_R \approx 1/100$ and normalized current waveforms for several values of τ_{TS} for fixed $\tau_{DS}/\tau_{TS} = 2$, from which the effective transit time is $T'_R = 3T_R$. The trap controlled mobility approximation shows good agreement with MC simulation for $\tau_{TS}/T_R < 100$ (blue curve represents both MC simulation and mentioned approximation, which are identical, the same holds for green curve). These curves have a characteristic plateau around $t = T_R$ with height, which is found from (3.19) divided by I_0 when $t \to +\infty$

$$\frac{\tau_e}{\tau_{DS}} = \frac{\tau_{TS}}{\tau_{TS} + \tau_{DS}}. \tag{3.36}$$

For $\tau_{TS}/T_R > 1/30$ the trapping is not strong enough (there are to few trapping and detrapping events) to fulfill the Central limit theorem and approximation fails (orange curve representing MC simulation differs significantly from black curve representing mentioned approximation for same parameters). Red curve is normalized current waveform for the detector with no trapping, which has $t_r = T_R$.

It is important to point out that the value of detrapping time τ_{DS} does not affect the validity of this approximation, because with increasing value of τ_{DS} the trap just holds the carriers longer, which increases the effective transit time T'_R, but does not change the number of trapping/detrapping events that happen before particle leaves the sample $\eta(T'_R)$ (see (3.26)), which depends on trapping time

$$\eta(T'_R) = \frac{T_R}{\tau_{TS}}. \tag{3.37}$$

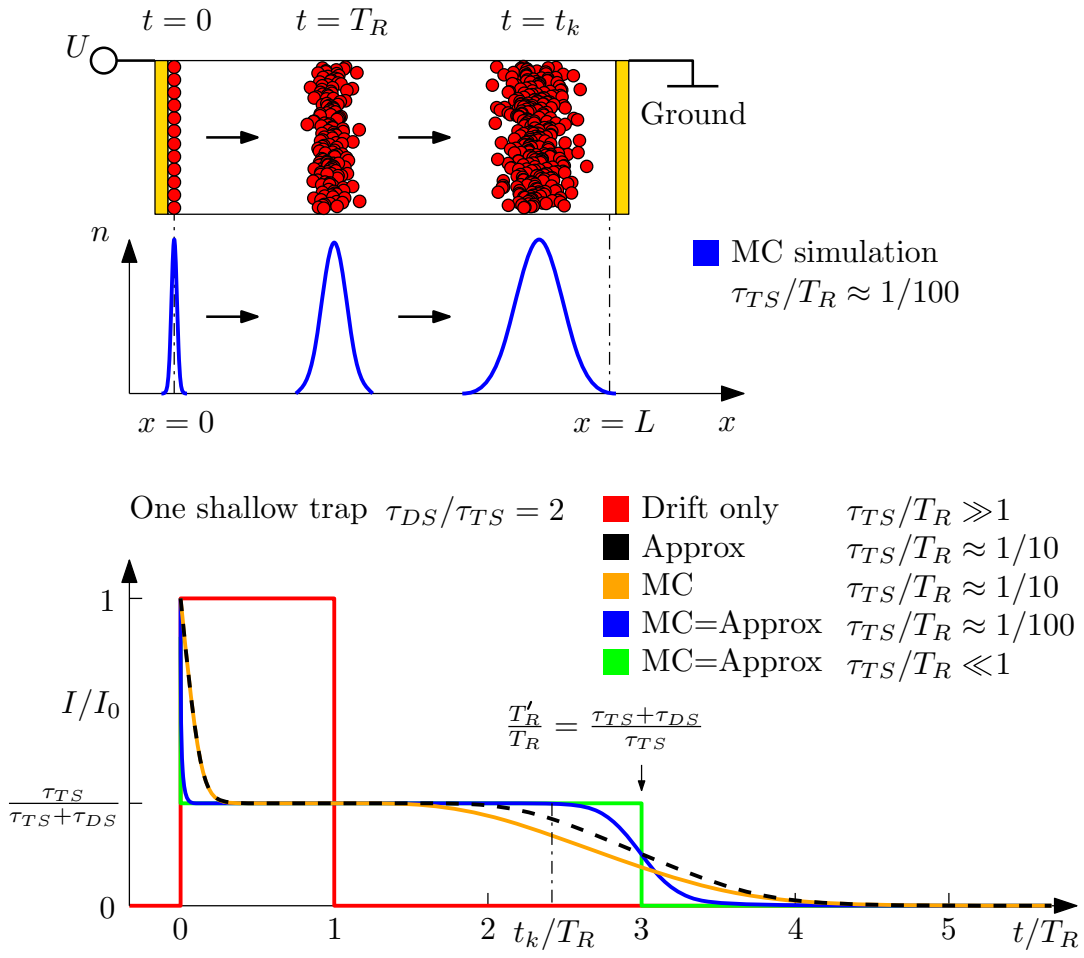

Figure 3.6: **Top**: MC simulation of the electron cloud evolution in the detector with the shallow trap at three different times. **Bottom**: Normalized current waveforms. Monte Carlo simulation is labeled *MC* and trap controlled mobility approximation is labeled *Approx*.

3.7.2 Approximation of a weak shallow trap

In case of $\tau_{TS}/T_R > 1$ majority of carriers are not trapped and rest of them are trapped mostly only once. This leads to effective separation of carriers into two groups. The first group are carriers that are never trapped and arrive to the anode in time T_R and they don't contribute to current for time $t > T_R$. The second group are carriers that are trapped at least once, and then are re-emitted into the conduction band, only these carriers contribute to the current for $t > T_R$. The initially free carriers are being trapped effectively generating exponential distribution of trapped electrons, which wait on average detrapping time τ_{DS} in the trap and lag behind free electrons. The probability of detrapping has exponential distribution (see subsection 3.3.2) and thus as trapped electrons are detrapped, they generate exponential distribution of detrapped electrons. When the never trapped electrons leave the detector at $t = T_R$, the current sharply falls to the value corresponding to the motion of the detrapped electrons for $t > T_R$. The contribution to current from detrapped carriers can be found from current waveform of exponential electron cloud, which is discussed in appendices (see equation (A.6)). The current waveform comprises of two components

$$I(t) = I_1(t)\chi_{[0,T_R]}(t) + I_2(t - T_R)\,\Theta(t - T_R), \tag{3.38}$$

where $I_1(t)$ is the analytical solution (3.19) valid for $t < T_R$

$$I_1(t) = \frac{Q_0}{T_R}\left[\frac{\tau_e}{\tau_{DS}} + \frac{\tau_e}{\tau_{TS}}\exp\left(-\frac{t}{\tau_e}\right)\right], \tag{3.39}$$

and $I_2(t)$ is the current of detrapped electrons valid for $t > T_R$

$$I_2(t) = [I_1(T_R) - \Delta I]\exp\left(-\frac{t}{\tau_b}\right), \tag{3.40}$$

where ΔI is the current from carriers that are never trapped at $t = T_R$ given by

$$\Delta I = \frac{Q_0}{T_R}\exp\left(-\frac{T_R}{\tau_{TS}}\right). \tag{3.41}$$

Current waveform (3.38) has a discontinuity at $t = T_R$ which is caused by collection of never trapped carriers and equal to ΔI. Parameter τ_b in (3.40) is the effective decay time of current from detrapped electrons defined by

$$\tau_b = \tau_{DS} + \frac{1}{2}\frac{T_R}{\tau_{TS}}\tau_{DS}, \tag{3.42}$$

where τ_{DS} is the average time that a carrier spends in the shallow trap and T_R/τ_{TS} is the average number of trapping events occurring during the traversal of the detector (see equation (3.37)). The last term in (3.42) represents the average lag of trapped electrons in shallow trap.

The MC simulation of the electron cloud evolution in the detector with one shallow trap $\tau_{TS}/T_R \approx 1$, $\tau_{DS}/\tau_{TS} \approx 1/10$ and in the detector without traps is shown in figure 3.7, where the electron cloud only drifts in the detector without traps while in the detector with one shallow trap the electron cloud consists of never trapped electrons and detrapped electrons (see the tail of the electron cloud in left bottom part). The normalized current waveform of shallow trap approximation (3.38) (labeled *Approx*), which is identical to the normalized current waveform obtained from MC simulation (labeled *MC*) has discontinuity ΔI at $t = T_R$ from collection of never trapped electrons. The contributions of never trapped electrons (black curve) and detrapped electrons (green curve) are also shown.

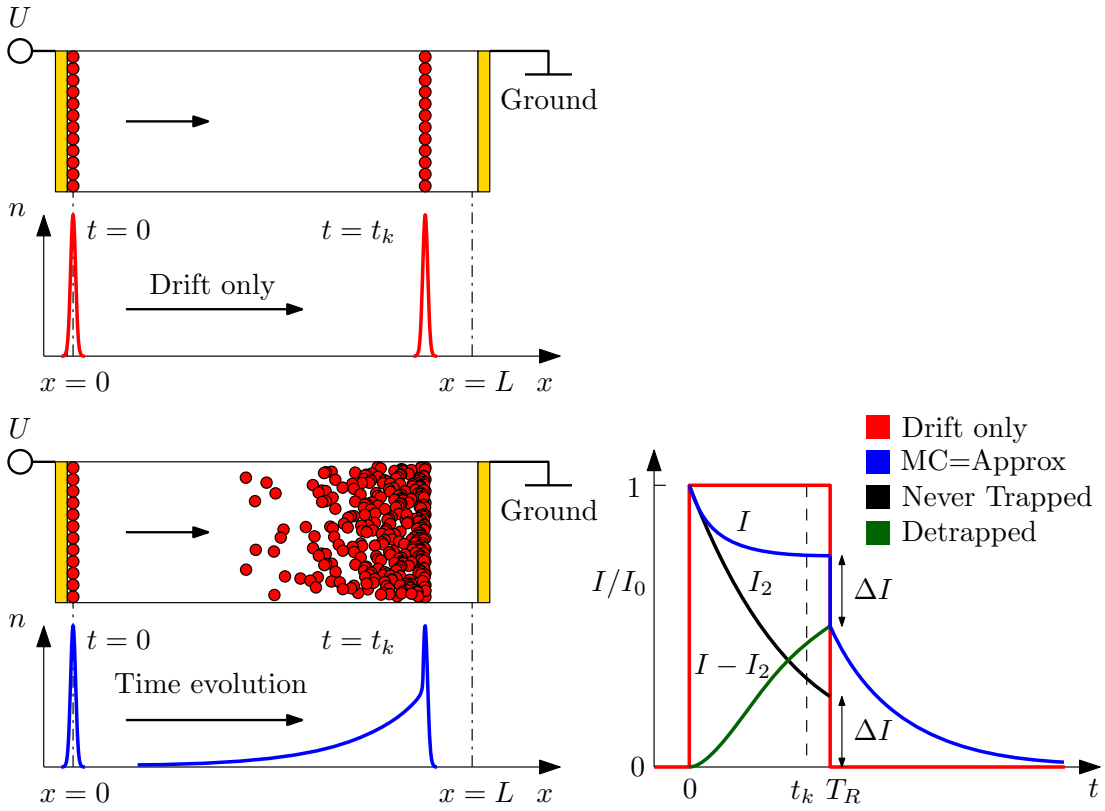

Figure 3.7: **Left top**: MC simulation of the electron cloud evolution in detector without traps at time $t = 0$ and $t = t_k$ with normalized electron concentration (red curve). **Left bottom**: MC simulation of the electron cloud evolution in detector with the shallow trap at time $t = 0$ and $t = t_k$ with normalized electron concentration (blue curve). **Right bottom**: Normalized current waveforms.

Current waveform (3.38) was tested using MC simulation. In figure 3.8, there are shown normalized current waveforms for several values of τ_{TS} for fixed $\tau_{DS}/\tau_{TS} = 1$. The weak shallow trap approximation shows good agreement with MC simulation for $\tau_{TS}/T_R > 1$, where relatively large discontinuity ΔI is present (blue curve represents both MC simulation and mentioned approximation, which are identical. The same holds for green curve). For $\tau_{TS}/T_R < 1$ the trapping is to fast (shallow trap is no longer weak, current discontinuity disappears $\Delta I \to 0$ and electron cloud thermalizes with the trap), approximation fails and MC simulation is needed to obtain correct current waveform. (orange curve representing MC simulation differs significantly from black curve representing shallow weak trap approximation for same parameters). Red curve is normalized current waveform for the detector with no trapping, which has $t_r = T_R$.

It is important to point out that the value of detrapping time τ_{DS} does not affect the validity of this approximation, because with increasing value of τ_{DS} the trap just holds the carriers longer, which increases the effective transit time T'_R, but does not change the number of trapping detrapping events that happen before particle leaves the sample, which depends on trapping time $\eta(T'_R) = \frac{T_R}{\tau_{TS}}$ (see equation (3.26)).

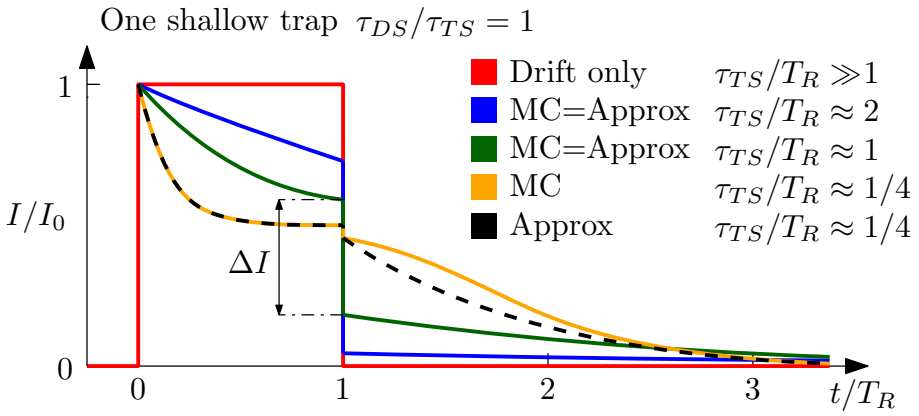

Figure 3.8: Current waveforms for the detector with one shallow trap for several values of τ_{TS} with discontinuity ΔI at $t/T_R = 1$. Monte Carlo simulation is labeled *MC* and the weak shallow trap approximation is labeled *Approx*.

3.7.3 Current waveform analysis

With the knowledge of two approximations that were discussed in previous subsections we can analyze current waveforms of the detector with one shallow trap. This discussion is based on [16]. Normalized current waveforms of the detector with one shallow trap for several values of τ_{TS} and fixed $\tau_{DS}/\tau_{TS} = 2$ (from which $T'_R/T_R = 3$) are shown in figure 3.9, where except the red curve (limit with no trapping) all other curves have initial high-current spike at short times, which corresponds to the drift of free electrons with microscopic mobility that is much larger than the effective (trap-controlled) drift mobility with which electrons move when they reach thermal equilibrium with shallow trap (orange and light green curve), these current waveforms have the characteristic plateau around $t = T_R$, its height is given by constant term in (3.19) and have effective transit time T'_R, this is when the trap controlled mobility approximation of electron cloud can be used (see subsection 3.7.1). The blue, dark green and purple curves show (unlike orange and light green curve) discontinuity in current ΔI at $t/T_R = 1$ caused by collection of significant amount of electrons that are never trapped, which are moving with drift velocity proportional to the microscopic drift mobility rather the effective drift mobility, this is when the weak shallow trap approximation can be used (see subsection 3.7.2). For $t/T_R < 1$ analytical solution (3.19) can be used. MC simulation or approximations must be used for $t/T_R > 1$. MC simulation allows to obtain current waveforms for any parameters of shallow trap. Since the detector doesn't have deep trap, all photogenerated carriers will eventually be collected, the total collected charge

$$Q_c = \int_0^{+\infty} I(t)\mathrm{d}t = Q_0, \tag{3.43}$$

which is independent on shallow trap parameters (in figure 3.9 all current waveforms have the same integral). When the initial distribution of carriers is not a delta function or when surface recombination is present, the current spike might not be visible in current waveform and to find current waveform MC simulation is needed.

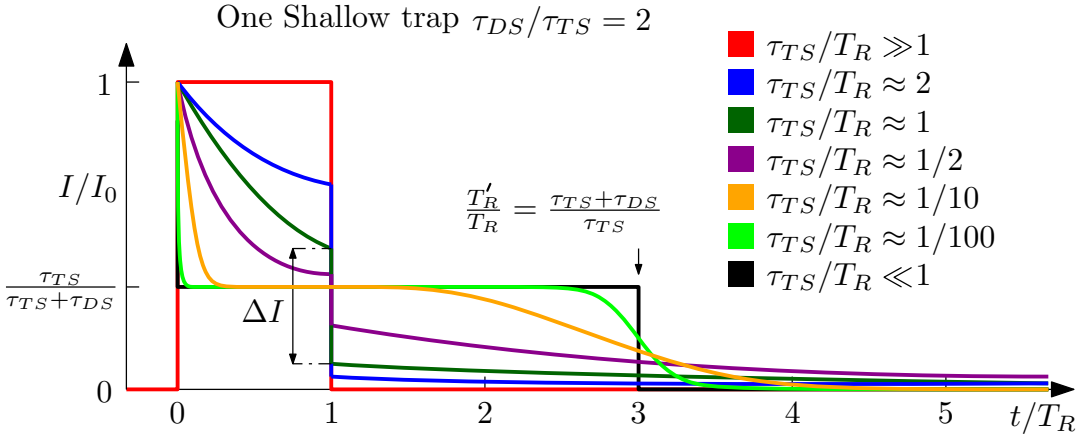

Figure 3.9: Normalized current waveforms of detector with shallow trap.

4. Experiment

4.1 Spectroscopic measurements

Radiation detectors most often work in the pulse mode, in which the detector records each individual quantum of radiation that generated e-h pairs inside the detector [1]. Accumulation of many events is needed for pulse processing. Each impact of radiation quantum creates current burst, which is integrated into charge Q and amplified in charge sensitive pre-amplifier, producing voltage step V_{max} proportional to Q. The voltage step is reshaped and again amplified by shaping amplifier, which converts the voltage step with variation δV into Gaussian with its center V_{max} with the full width at half maximum $FWHM = \delta V$. The output of the shaping amplifier is then processed in multi-channel analyzer (MCA) and recorded in computer. Detector has two opposite planar electrical contacts. Scheme of the spectroscopic measurement is shown in figure 4.1. Experimental setup consists of shielding vacuum chamber (to prevent loss of energy of radiation source), in-house created preamplifier based on Amptek A250 preamplifier, shaping amplifier Ortec 671, multi-channel analyzer Ortec MCA easy, high voltage source Iseg SHQ 122M and computer with in-house created program for complex spectra evaluation. The detector is placed inside the vacuum chamber with the radiation source pointing at the cathode. Spectroscopic measurements for strongly absorbed radiation are often evaluated using Hecht equation

$$Q(U) = Q_0 \frac{\mu_e \tau U}{L^2} \left[1 - \exp\left(\frac{-L^2}{\mu_e \tau U} \right) \right], \tag{4.1}$$

where Q_0 is the initial radiation generated charge, U is the applied bias and τ is the lifetime of electrons, which is in the context of the detector with deep trap equal to τ_{TD}. Equation (4.1) is the special case of Hecht equation for one-carrier type (electrons) [28]. For given bias U the charge collection efficiency CCE is defined as

$$CCE(U) = \frac{Q(U)}{Q_0}. \tag{4.2}$$

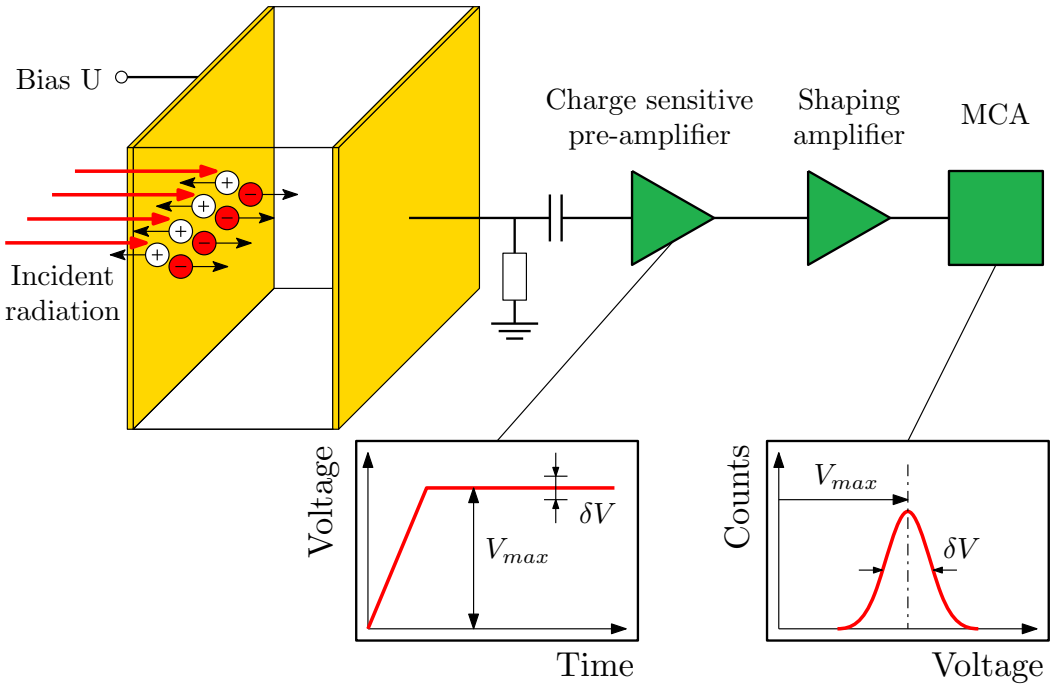

Figure 4.1: Scheme of the setup for radiation spectra measurement.

4.2 Laser-induced Transient Current Technique

Laser-induced Transient Current Technique (L-TCT) is based on above band-gap laser pulse illumination, where the light is strongly absorbed. The laser pulse is used as an external source generating electron-hole (e-h) pairs near under the illuminated electrode, e-h pairs are separated by electric field and drift toward corresponding electrodes. Detector has two planar opposite electrodes (same geometry is used in spectroscopic measurements). Electron movement induces electric current through the collecting electrode, which is amplified using current sensitive amplifier and measured on digital sampling oscilloscope. Possibility of triggering on laser pulse significantly decreases noise compared to untriggered sources like alpha particle, since many events need to be accumulated for pulse processing. We can also use additional illumination of cathode or anode using continuous LED with 660 nm wavelength to generate additional space charge to study space charge limited current. This LED is otherwise turned off. Scheme of the simplified L-TCT setup is shown in figure 4.2. In our configuration positive bias is applied to the illuminated electrode, and generated holes are immediately collected while electrons drift though the whole bulk material. Experimental setup consists of above band-gap pulsed laser diode (660 nm wavelength, 300 mW maximum pulse peak power, 1 ns pulse width as FWHM), which is powered by Picosecond Lab pulse generator with repetition rate (1 Hz – 100 kHz), high frequency voltage amplifier (L–3 Narda–Miteq AM–1607–3000) and ultrafast digital sampling oscilloscope (LeCroy WaveRunner 640Zi, 40 Gs/s, resolution up to 11 bits, 4 GHz bandwidth, DC input impedance). For more detail of setup see [29]. In-house made bias switching unit is used for generation of bias pulses, which are synchronized with laser pulse using function generator (AFG3252, sampling rate 2 GS/s). Laser pulse delay after the rise time of bias pulse can be varied, which

allows observing formation of space charge inside the detector. Depolarization time, that is the time when no bias is applied on the detector, is needed, for depolarization of the detector. Scheme of the laser pulse and bias pulse relative position is shown in figure 4.3. Measured current waveforms are systematically distorted by the transfer function of used electronic circuit. Deconvolution procedure is used to obtain original current waveforms. Details of the deconvolution procedure are discussed in [29].

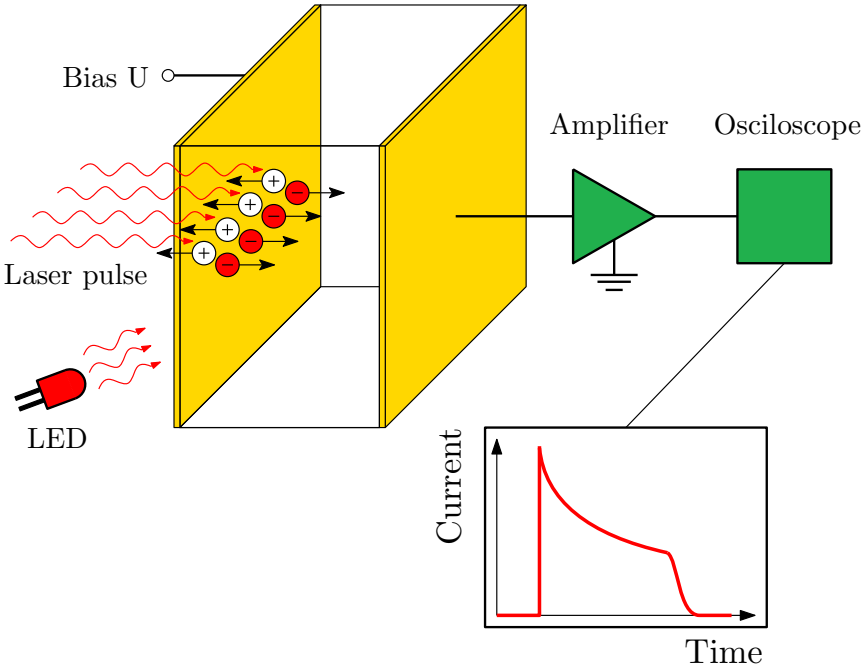

Figure 4.2: Scheme of the L-TCT setup.

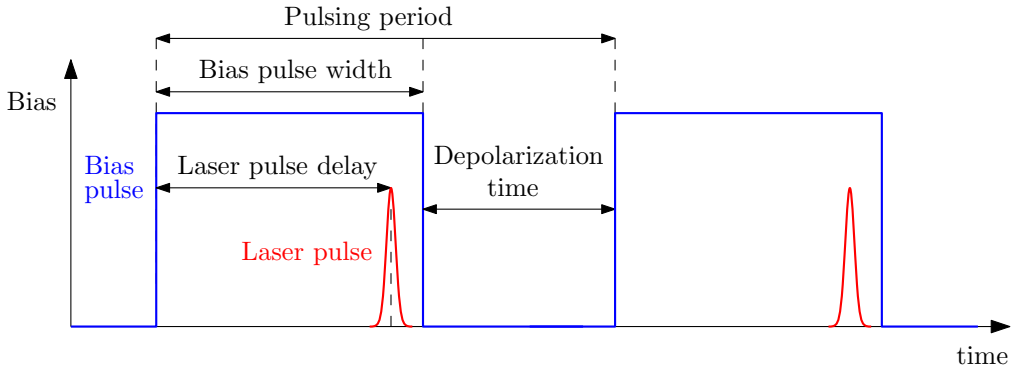

Figure 4.3: Scheme of the bias pulsing.

5. Results and discussion

5.1 Detector preparation

Detectors prepared from semi-insulating (SI) GaAs and CdZnTe single crystals were used in this work. Chromium compensated SI GaAs was prepared from the Liquid Encapsulated Czochralski material in Tomsk State University, Russia, using the diffusion of chromium evaporated on the surface of the detector. SI CdZnTe was prepared by the high pressure Bridgman technique. The dimension of the GaAs detector was 4 mm $\times$ 4 mm $\times$ 0.5 mm while for CdZnTe was 5 mm $\times$ 5 mm $\times$ 1.46 mm. Electrical contacts on GaAs detector were prepared using sputtering technique while on CdZnTe detector electrical contacts were prepared by electroless deposition from aqueous solution of gold chloride.

5.2 Spectroscopic measurements

Spectroscopic measurement setup is described in detail in section 4.1. Radiation source of α-particles ^{241}Am (Energy of main line 5480 keV, radioactive activity 8.4 kBq) was used for measurement. Only signal of electrons is measured for both GaAs and CdZnTe detectors, since in case of holes no signal was detected. Collected charge is proportional to the position of the channel with maximum counts. Measured α-spectra for GaAs detector are shown in figure 5.1, where in the inset the position of the maximum of each spectrum (fitted by the Gauss function) is plotted against the corresponding bias. This dependence is fitted by the Hecht equation (4.1). It is clearly seen in figure 5.1, that the fit does not correctly represent measured dependence, because the presence of plasma effect screens of the external electric field, which results in (e-h) pair recombination [30]. Measured α-spectra for CdZnTe detector are shown in figure 5.2, where in the inset the position of the maximum of each spectrum is plotted against the corresponding bias. This dependence is fitted by the Hecht equation (4.1). In case of CdZnTe detector Hecht equation correctly describes measured dependence with typical saturation of collected charge. From Hecht equation we get for CdZnTe detector $\mu\tau = 2.0 \cdot 10^{-3}$ cm^2/V. To evaluate more charge transport parameters of GaAs and CdZnTe detectors L-TCT will be used.

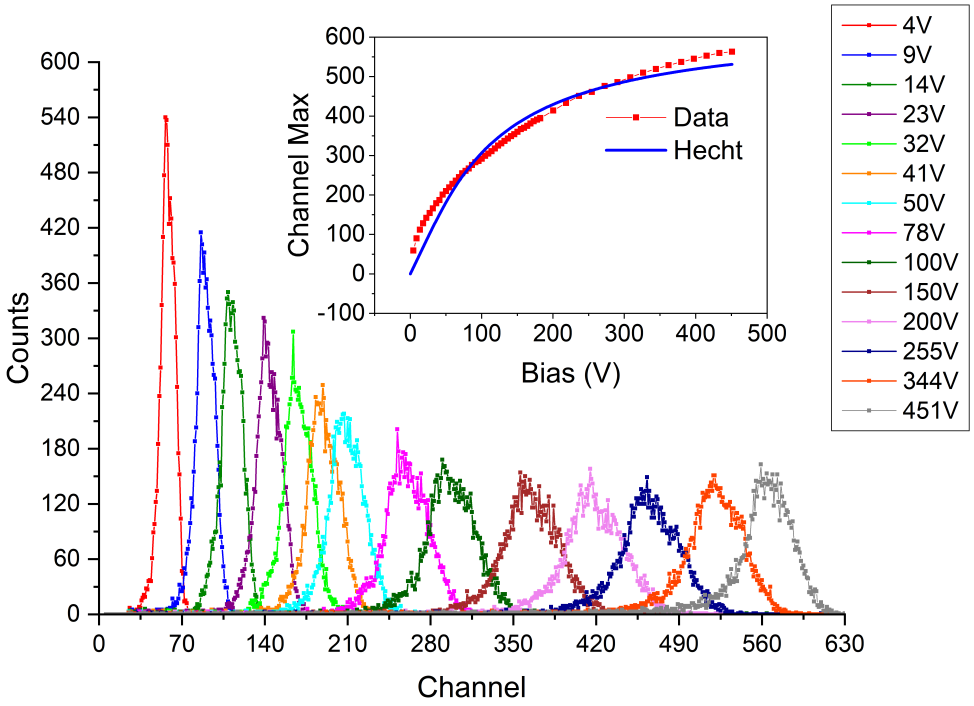

Figure 5.1: Pulse height spectra of $\alpha-$source ^{241}Am for GaAs detector. **Inset**: Bias dependence of collected charge and Hecht equation fit.

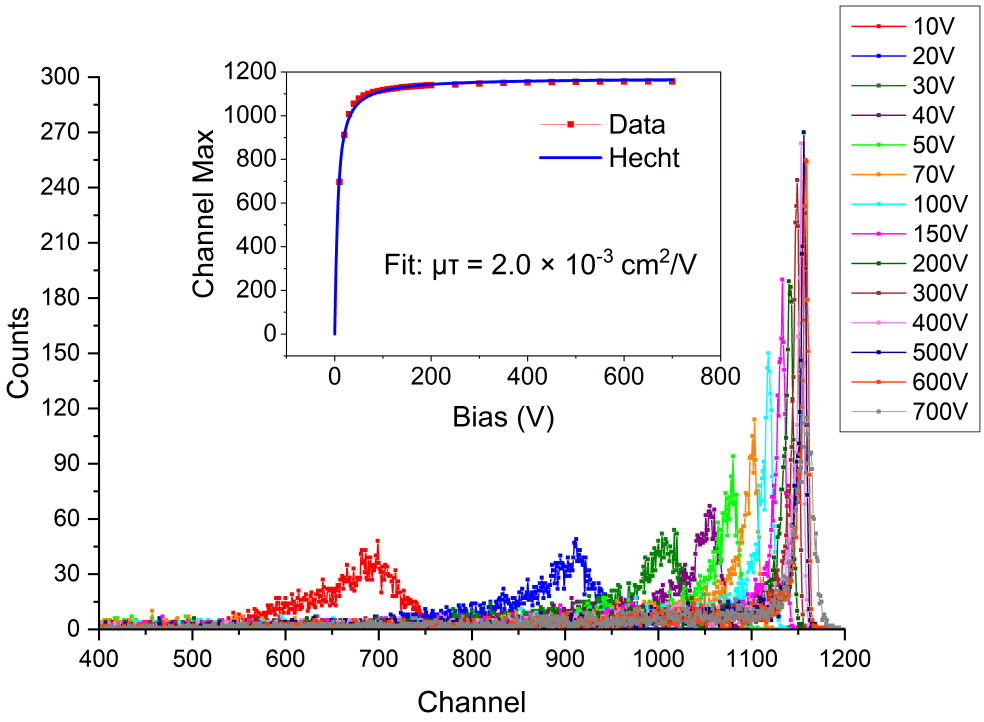

Figure 5.2: Pulse height spectra of $\alpha-$source ^{241}Am for CdZnTe detector. **Inset**: Bias dependence of collected charge and Hecht equation fit.

5.3 Laser-induced Transient Current Technique

L-TCT measurement setup was described in section 4.2. Current waveforms only for electrons were measured, since no signal of holes was detected. Detector itself is kept in dark during measurement and only dark current flows through the detector. Size of the laser pulse illuminated area on the anode is about 3 mm^2 and detector walls without electrodes were shielded by mask to prevent unintentional illumination. Neutral density filter was used to attenuate laser pulse intensity to prevent a disturbance in electric field so the laser pulse acts as a probe. Measurements for GaAs and CdZnTe detectors were done with DC and pulsed bias (pulsing period 20ms, laser pulse delay 100μs and bias pulse width 5ms). Details about laser pulse and bias pulse synchronization are shown in section 4.2.

5.3.1 GaAs

Bias dependence of current waveforms for GaAs detector with pulsed bias together with MC simulation (labeled MC) are shown in figure 5.3, where electric field depicted in the inset, was determined using MC simulation described in chapter 3. Laser pulse delay 100μs after the rise time of bias pulse is short enough so the detector is still unpolarized. It was found that observable detector polarization occurs for the laser pulse delay longer than 150μs. In unpolarized detector, where the space charge density $\rho(x) = 0$ the internal electric field is constant (see section 2.7). Bias pulsing is needed to separate contributions of electric field and trapping phenomena to the current waveform and for correct evaluation of transport parameters. Bias dependence of current waveforms normalized by corresponding bias is shown in figure 5.4, where it is clearly seen that current waveforms lie on each other in overlapping intervals, from which we can conclude that GaAs detector does not have surface recombination (for details see section 2.9). From bias dependence of current waveforms for unpolarized detector (with pulsed bias) with knowledge of that no surface recombination occurs, detector transport parameters, which are shown in table 5.1, were obtained from MC simulation. One shallow trap with trapping/detrapping time $\tau_{TS} = 250$ ns, $\tau_{DS} = 40$ ns and one deep trap with trapping time $\tau_{TD} = 150$ ns, respectively were evaluated from MC simulation. Detrapping time of the deep trap τ_{DD} cannot be determined from measured current waveforms since $\tau_{DD} \gg T_R$ and on the time scale of T_R no detrapping from the deep trap occurs for all values of applied bias. MC simulation shows excellent agreement with measured current waveforms. Shallow trap in GaAs with $\tau_{TS} = 250$ ns, $\tau_{DS} = 40$ ns can be classified as a weak shallow trap, which causes tail of the current waveform beyond T_R (see subsection 3.7.2). Evaluated electron drift mobility from MC simulation is $\mu_e = 3625$ cm^2/Vs while the mobility evaluated directly from (2.13), where T_R is replaced with transit time t_r (taken from rise edge of current waveform to the inflection point of falling edge) is $(\mu_e)_{tr} = 3510$, which is less than μ_e evaluated form MC simulation, which is caused by the shallow trap that extends transit time and thus decrease measured mobility from transit time $(\mu_e)_{tr}$.

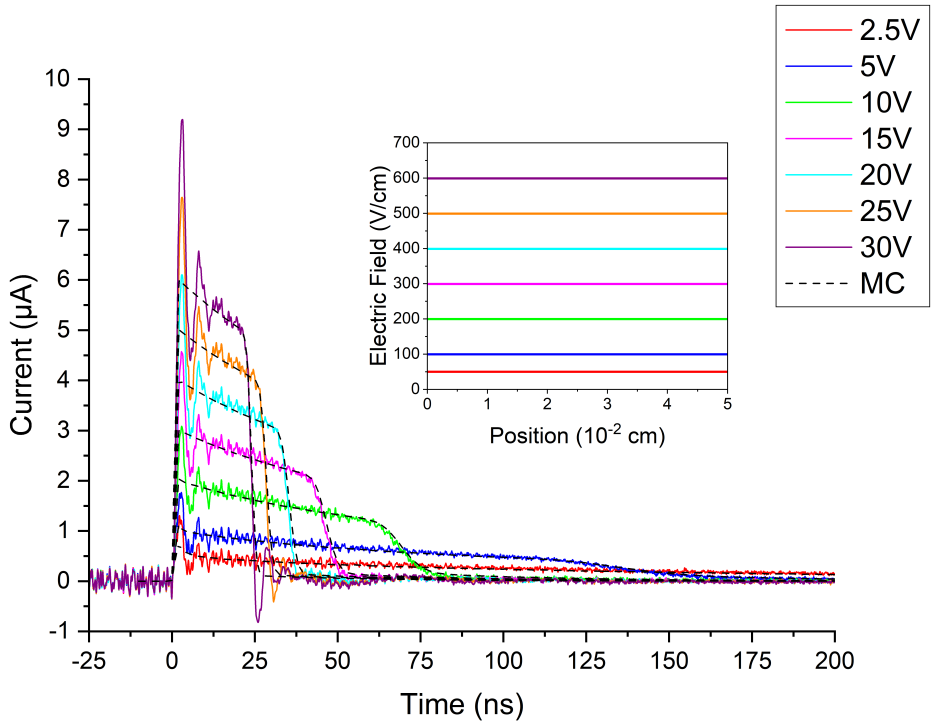

Figure 5.3: Bias dependence of current waveforms of GaAs detector using pulsed bias. **Inset**: Internal electric field.

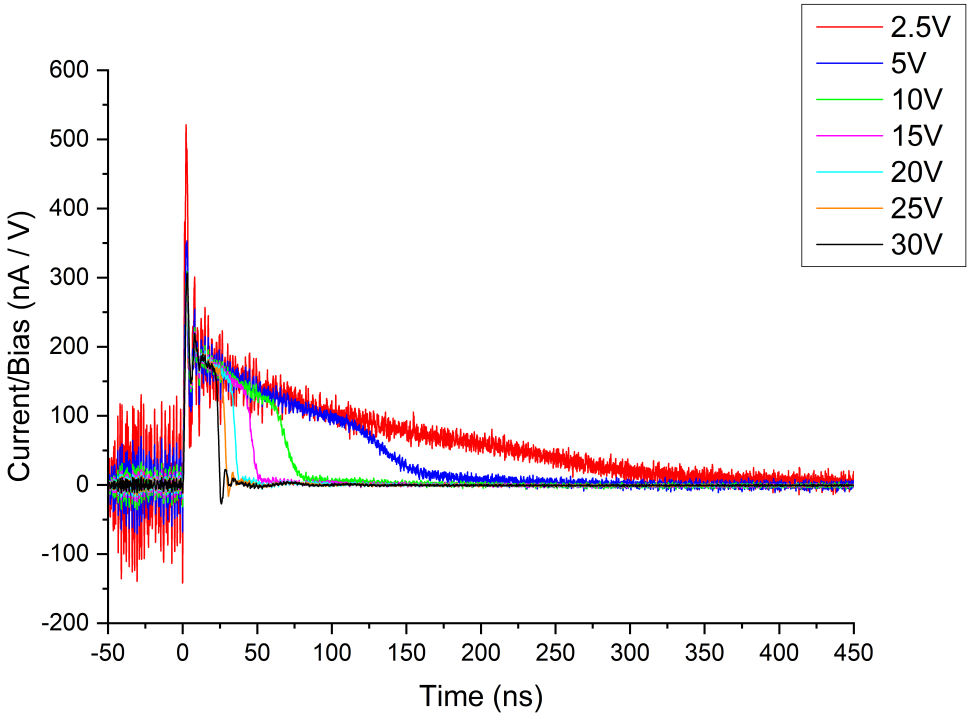

Figure 5.4: Bias dependence of current waveforms normalized by respective bias of GaAs detector using pulsed bias. **Inset**: Internal electric field.

Table 5.1: Detector transport parameters from MC simulation.

Material	GaAs	CdZnTe
L (cm)	0.05	0.146
Q_0 (fC)	130	47
μ_e (cm^2/Vs)	3625	1050
D_e (cm^2/s)	92	26
τ_{TD} (ns)	150	2000
τ_{DD} (ns)	$\gg T_R$	$\gg T_R$
τ_{TS} (ns)	250	13
τ_{DS} (ns)	40	1.1

Hecht eqaution can be applied to the bias dependence of collected charge (equal to the time integral of current waveform) for the unpolarized detector with pulsed bias to obtain $\mu\tau$ product. This is shown in figure 5.5, where the dependence of the collected charge on applied bias is shown with Hecht relation in inset. Hecht equation in this case (unlike in case of spectrscopic measurements with $\alpha-$particles) correctly fits the measured dependence. Determined $(\mu\tau)_{LTCT} = 5.9 \cdot 10^{-4}$cm^2/V, which can be compared with parameters obtained from MC simulation of current waveforms ($\mu_e = 3625$ cm^2/Vs and trapping time of the deep trap $\tau_{TD} = 150$ ns) to get $\mu_e\tau_{TD} = 5.4 \cdot 10^{-4}$cm^2/V, which is a good agreement and demonstrates that individual transport parameters can be obtained from L-TCT.

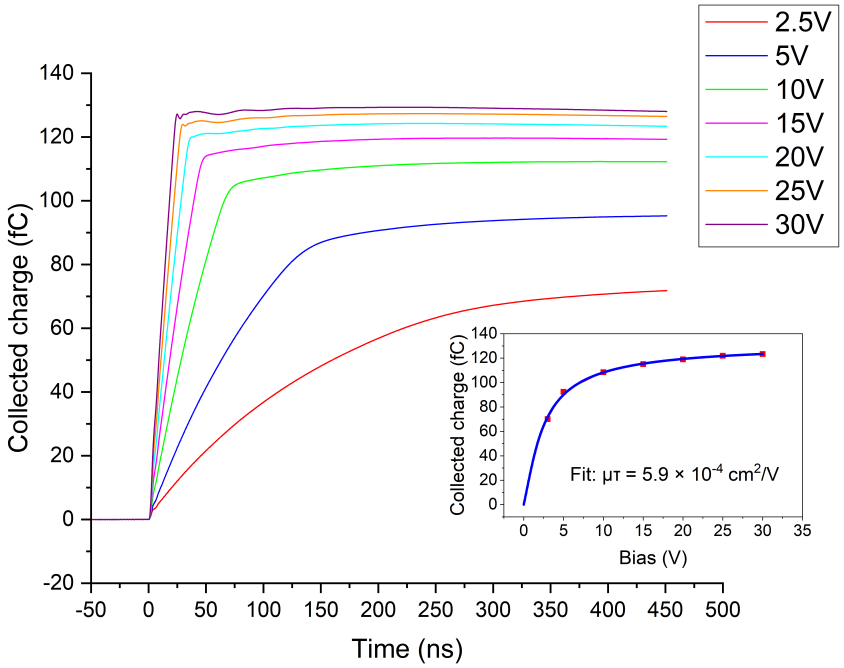

Figure 5.5: Bias dependence of collected charge calculated from current waveforms of GaAs detector using pulsed bias. **Inset**: Bias dependence of collected charge and Hecht equation fit.

Measured current waveforms for GaAs detector with DC bias are shown in figure 5.6, where electric field (shown in inset) was evaluated from MC simulation using the same parameters, which were previously obtained from MC simulation of measurement with pulsed bias. Slope of the electric field is increasing with increasing bias without observable saturation in the measured bias interval. Maximum of the electric field is for all bias values approximately in the center of the detector. In our L-TCT setup higher values of applied bias make current waveform transit time too short and used electronic circuit starts to oscillate, which prevents measurement.

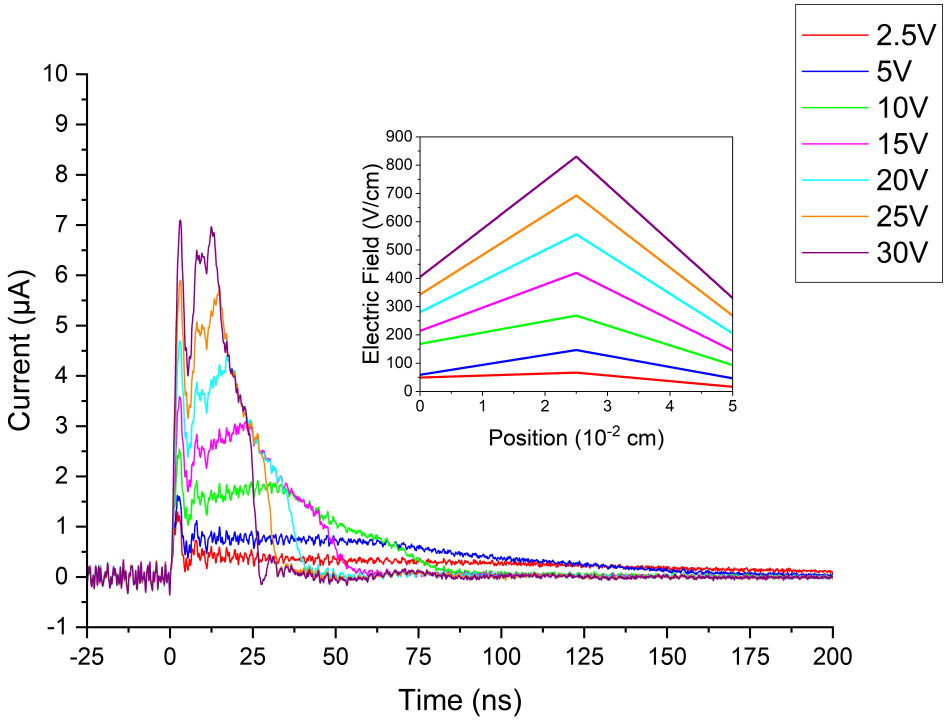

Figure 5.6: Bias dependence of current waveforms of GaAs detector using DC bias. **Inset**: Internal electric field.

Dependence of the current waveform shape on the laser pulse delay for GaAs detector with applied bias 30 V is shown in figure 5.7, where red curve represents current waveform of unpolarized detector and other curves represent detector with space charge. MC simulation is depicted by black dashed curves and is shown for unpolarized detector and for maximally polarized detector. MC simulation shows excellent agreement with measured waveforms. Internal electric field (shown in the inset) is constant for unpolarized detector (red curve) and for polarized detector electric field has increasing profile from cathode to the center of the detector, after which the electric field decreases to the anode. This electric field profile might be explained by variable conductivity in the detector material, which cannot be verified using only L-TCT and other measurements have to be used.

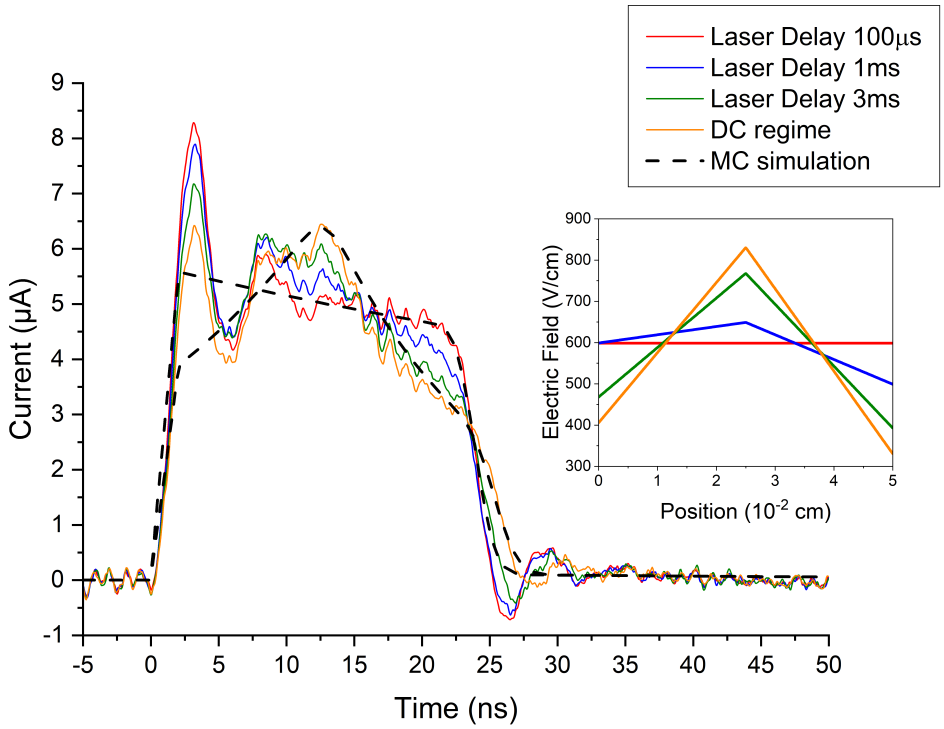

Figure 5.7: Dependence of the current waveform shape on the laser pulse delay for GaAs detector with applied bias 30 V. **Inset**: Internal electric field.

To demonstrate the detector with space charge limited current (SCLC), L-TCT with probing pulsed laser diode together with additional continuous above band gap LED was used. Continuous LED illumination of the detector cathode induces SCLC, which is described in subsection 2.7.5. Current waveforms are shown in figure 5.8, where red resp. blue curve represents current waveform with resp. without LED illumination of the detector with pulsed bias 15V. Internal electric field is depicted in the inset. SCLC produces square root electric field profile inside the detector, which was fitted using MC simulation (blue curve). MC simulation closely matches the measured current waveforms and shows applicability of our SCLC model.

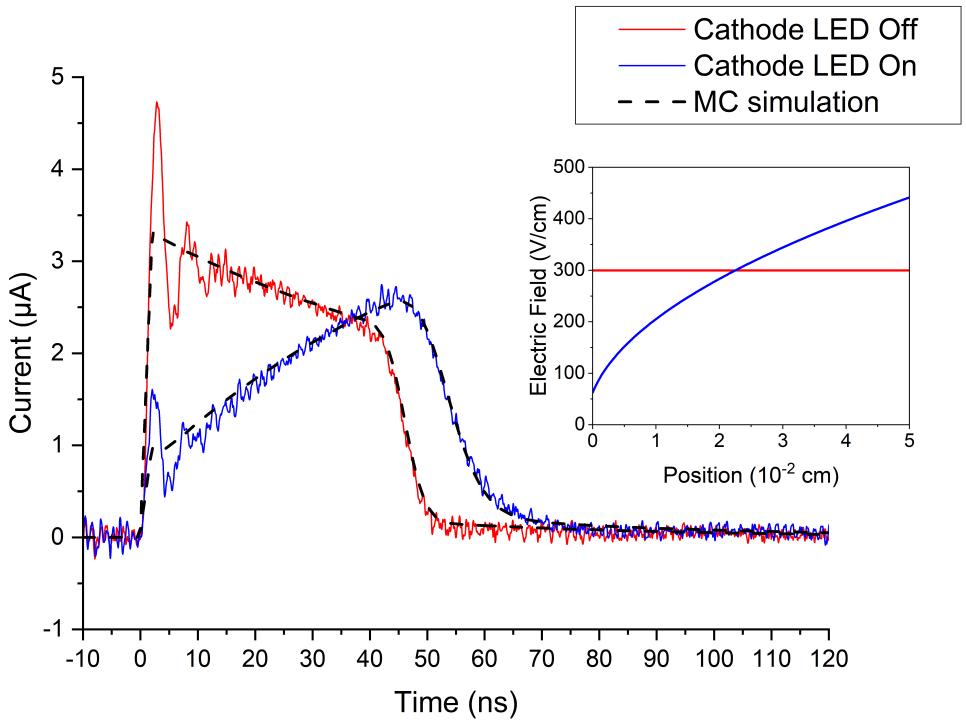

Figure 5.8: Current waveforms of GaAs detector with pulsed bias equal to 15V and additional LED illumination of cathode. **Inset**: Internal electric field.

To demonstrate formation of inactive layer in the detector, the continuous LED was used to illuminate detector anode. Measured current waveforms are shown in figure 5.9, where red resp. blue curve represents current waveform with resp. without LED illumination of the detector with pulsed bias 15V. Internal electric field is depicted in the inset. MC simulation was applied using previously determined parameters to find the internal electric field profile for the case of anode illumination. LED illumination creates additional e-h pairs under anode, which are separated in the electric field. Electrons are immediately collected by the anode while holes drift into the bulk. These holes produce positive space charge that creates inactive layer under the anode and simultaneously attracts electrons from cathode into the bulk causing negative space charge in the rest of the detector. Generated space charge produces the electric field profile shown in the inset of figure 5.9.

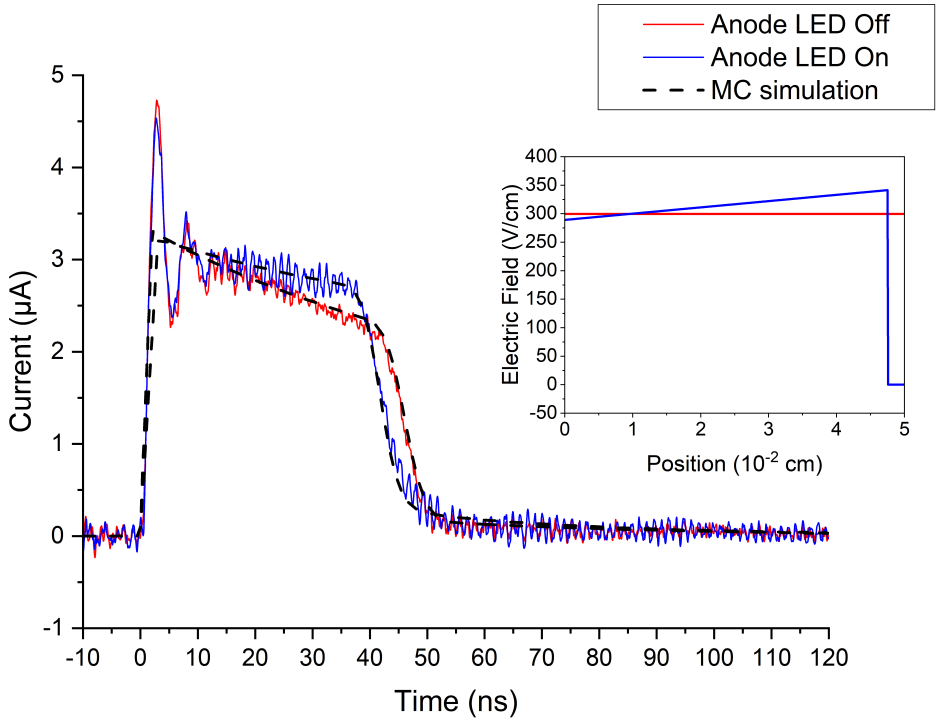

Figure 5.9: Current waveforms of GaAs detector with pulsed bias equal to 15V and additional LED illumination of anode. **Inset**: Internal electric field.

5.3.2 CdZnTe

Bias dependence of current waveforms for CdZnTe detector with pulsed bias together with MC simulation (labeled MC) are shown in figure 5.10, where the electric field (depicted in the inset) was determined using MC simulation described in chapter 3. Laser pulse delay 100μs after the rise time of the bias pulse is short enough so the detector is still unpolarized. It was found that observable detector polarization occurs for the laser pulse delay longer than 500μs. In unpolarized detector, where the space charge density $\rho(x) = 0$, the internal electric field is constant (see section 2.7). Bias pulsing is needed to separate contributions of electric field and trapping phenomena to the current waveform and for correct evaluation of transport parameters.

Bias dependence of current waveforms normalized by corresponding bias is shown in figure 5.11, where it is clearly seen that current waveforms lie on each other in overlapping intervals, from which we can conclude that CdZnTe detector does not have surface recombination (for details see section 2.9). From the bias dependence of current waveforms for unpolarized detector with knowledge that no surface recombination occurs, detector transport parameters, which are shown in table 5.1, were obtained from MC simulation. One shallow trap with trapping/detrapping time $\tau_{TS} = 13$ ns, $\tau_{DS} = 1.1$ ns and one deep trap with trapping time $\tau_{TD} = 2000$ ns were evaluated from MC simulation. Detrapping time of the deep trap τ_{DD} cannot be determined from measured current waveforms since $\tau_{DD} \gg T_R$ and on the time scale of T_R no detrapping from the deep trap occurs for all values of applied bias. MC simulation shows excellent agreement with measured current waveforms. Shallow trap in CdZnTe with $\tau_{TS} = 13$ ns, $\tau_{DS} = 1.1$ ns causes trap controlled mobility, which reduces electron drift mobility μ_e to effective mobility μ_{eff} (see subsection 3.7.1). Evaluated electron drift mobility from MC simulation is $\mu_e = 1050$ cm^2/Vs while the effective mobility calculated from (3.24) is $\mu_{eff} = 970$ cm^2/Vs. The electron mobility evaluated directly from transit time using (2.13), where T_R is replaced with transit time t_r (taken from rise edge of current waveform to the inflection point of falling edge) is $(\mu_e)_{tr} = 980$ cm^2/Vs, which is very close to the effective mobility, which is expected, since the measured transit time corresponds to the effective transit time T_R' rather than T_R (for details see subsection 3.7.1). Trap controlled mobility also causes trap controlled diffusion with effective diffusion coefficient D_{eff} (see its definition (3.31)), which is proportional to the square of the applied bias and for bias 100V is $D_{eff} = 38$ cm^2/s while ordinary diffusion coefficient $D_e = 26$ cm^2/s is bias independent and is obtained from Einstein relation (2.3). The effective diffusion is greater than ordinary diffusion for bias 100V . This trap controlled diffusion is the main proof of the presence of shallow trap, because the falling edge of the current waveform is broadened much more than without shallow trap. It is important to point out that the transfer function of the electronic circuit (mainly the high frequency limit of the circuit) can produce similar effect of current waveform edge broadening. This does not have measurable effect in our used L-TCT setup.

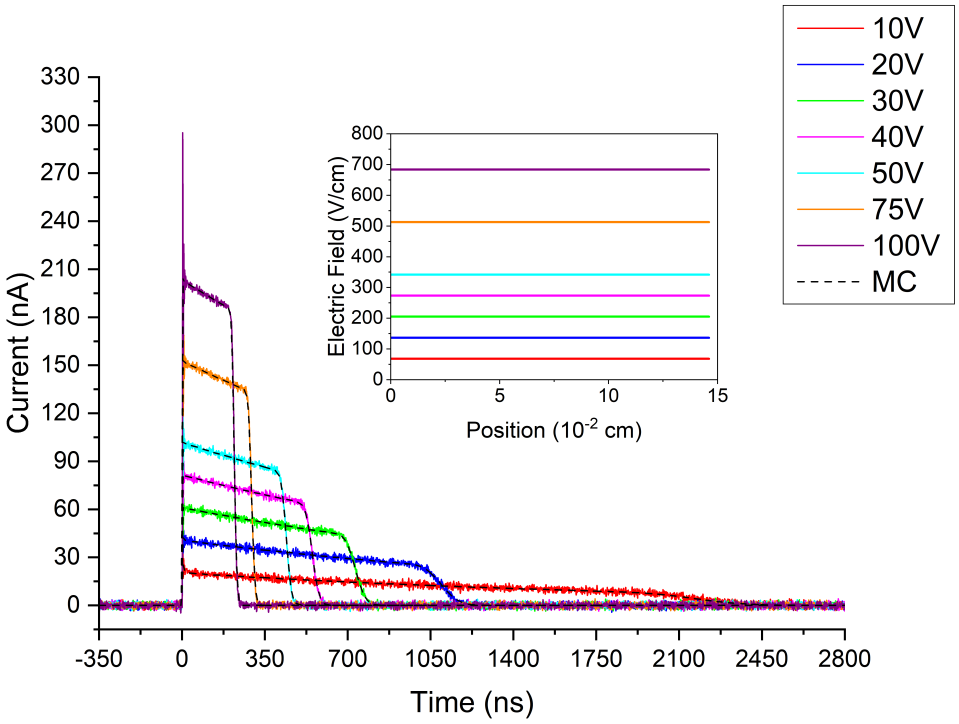

Figure 5.10: Bias dependence of current waveforms of CdZnTe detector for several values of pulsed bias. **Inset**: Internal electric field.

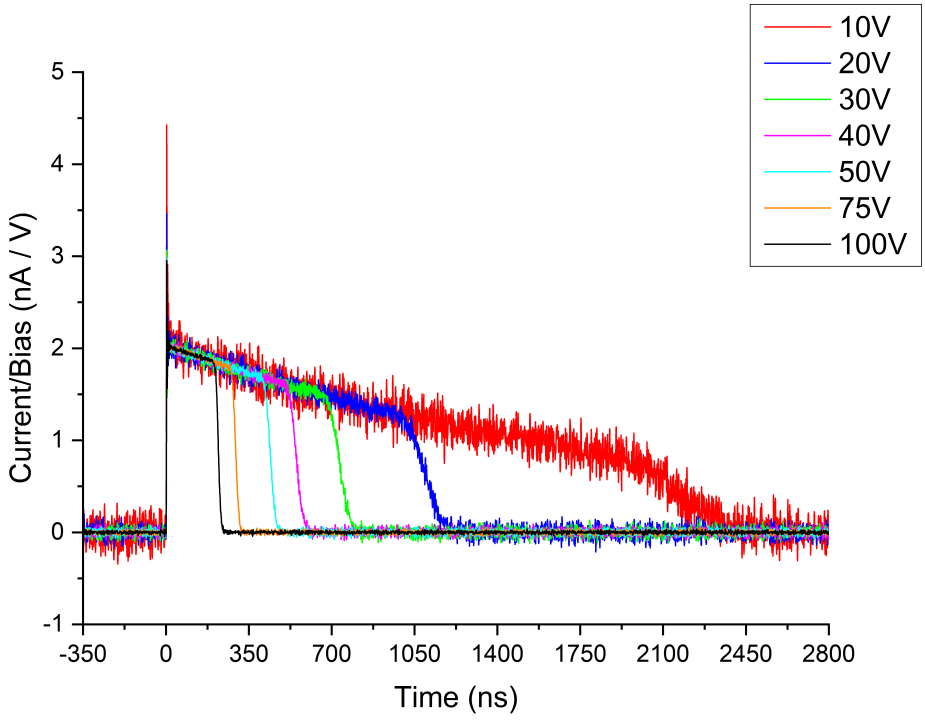

Figure 5.11: Bias dependence of current waveforms normalized by respective bias of CdZnTe detector using pulsed bias. **Inset**: Internal electric field.

Hecht eqaution can be applied to the bias dependence of collected charge calculated from integral of current waveform for the unpolarized detector with pulsed bias to obtain $\mu\tau$ product. This is shown in figure 5.12, where the dependence of the collected charge on applied bias is shown with Hecht relation in the inset. Hecht equation in this case correctly fits the measured dependence. Determined $(\mu\tau)_{LTCT} = 1.9 \cdot 10^{-3}\text{cm}^2/\text{V}$ can be compared with parameters obtained from MC simulation of current waveforms ($\mu_e = 1050$ cm^2/Vs and trapping time of the deep trap $\tau_{TD} = 2$ μs) to get $\mu_e\tau_{TD} = 2.1 \cdot 10^{-3}\text{cm}^2/\text{V}$. From spectroscopic measurements we evaluated $(\mu\tau)_\alpha = 2.0 \cdot 10^{-3}\text{cm}^2/\text{V}$. All evaluated $\mu\tau$ product for CdZnTe detector show good agreement, which further demonstrates the possibility to obtain transport parameters from L-TCT.

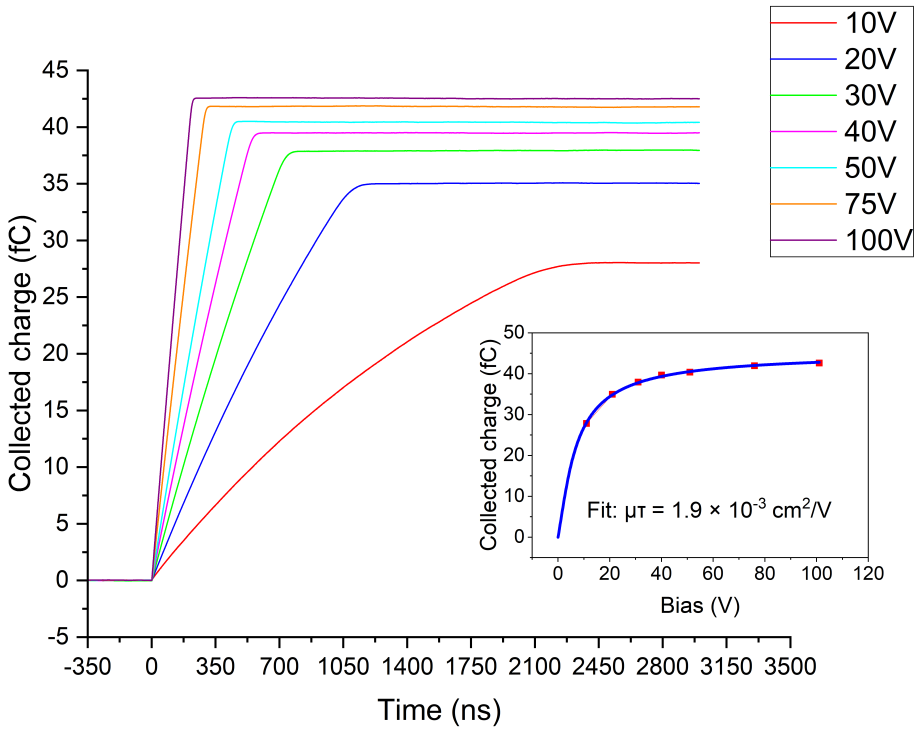

Figure 5.12: Bias dependence of collected charge calculated from current waveforms of CdZnTe detector using pulsed bias. **Inset**: Bias dependence of collected charge and Hecht equation fit.

Measured current waveforms for CdZnTe detector with DC bias are shown in figure 5.13, where electric field (shown in inset) was evaluated from MC simulation using the same parameters, which were previously obtained from MC simulation of measurement with pulsed bias. Internal electric field has linear profile and position independent space charge is present in the detector (see subsection 2.7.1). Slope of the electric field is increasing from $a_{10V} = 180$ V/cm^2 for bias 10V to $a_{100V} = 870$ V/cm^2 which saturates around 50V and does not increase in the measured bias interval. Bias dependent positive space charge density ρ is calculated from (2.63) with use of $\varepsilon_r = 10$ for CdZnTe and is for bias 10V $\rho_{10V} = 1.0 \cdot 10^9$ cm^{-3} and for 100V $\rho_{100V} = 4.8 \cdot 10^9$ cm^{-3}. This space charge can be completely removed using puled bias.

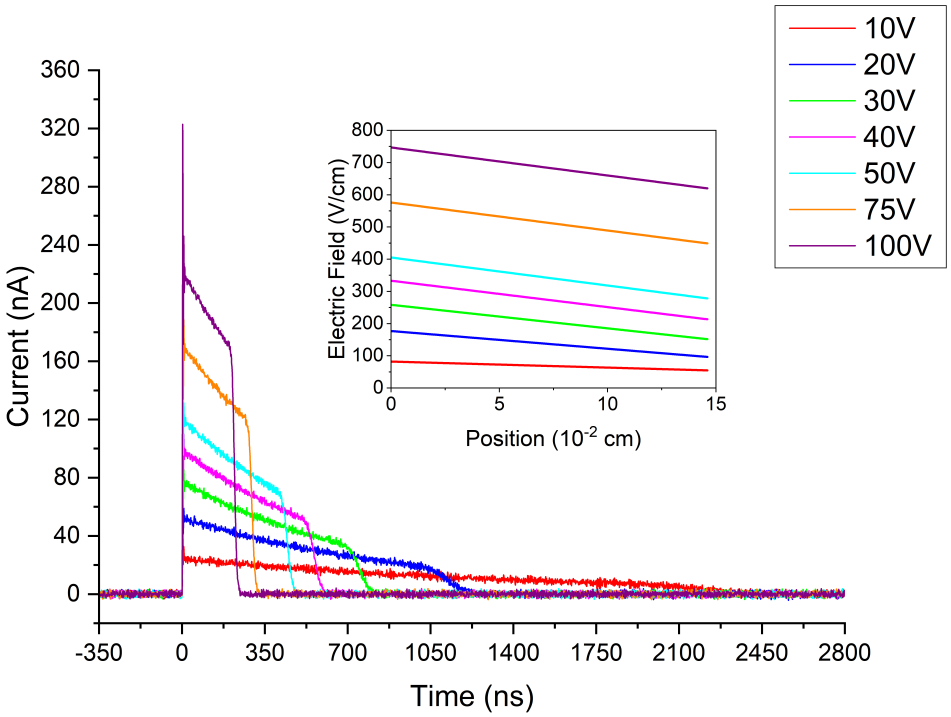

Figure 5.13: Bias dependence of current waveforms of CdZnTe detector using DC bias. **Inset**: Internal electric field.

Comparison of current waveforms of CdZnTe detector with pulsed and DC bias 30V is shown in figure 5.14, where red curve represents current waveform of unpolarized detector and blue represents polarized detector with space charge. MC simulation is depicted by black dashed curves and is shown for unpolarized and polarized detector. MC simulation shows excellent agreement with measured waveforms. Internal electric field (shown in the inset) is constant for unpolarized detector (red curve) and for polarized detector electric field has decreasing linear profile from cathode to the anode (blue curve).

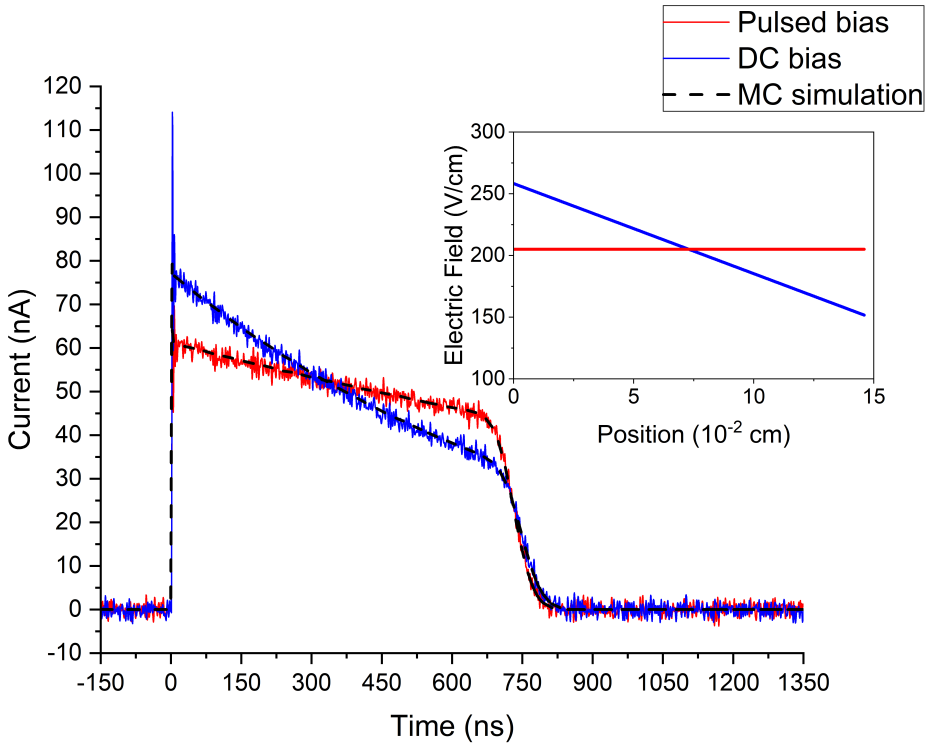

Figure 5.14: Current waveforms of CdZnTe detector with pulsed and DC bias equal to 30V. **Inset**: Internal electric field.

6. Conclusion

This thesis is focused on the study of charge transport in semiconducting radiation detectors. In theoretical part charge transport with diffusion is studied using continuity equation and drift-diffusion equation, from which the current waveform is calculated. Analytical solution of current waveforms for the detector with one shallow and one deep trap up to default transit time T_R is derived directly from kinetic equations for two level system. Effects of electric field on the charge transport are studied. Theoretical current waveforms for the detector with linear space charge density, region with constant space charge density, region with linear space charge density and for the detector with space charge limited current are derived together with exact profiles of electric field. Simple method to recognize the presence of surface recombination in the detector from the bias dependence of current waveforms normalized by corresponding bias is proposed. If the detector has surface recombination, normalized current waveforms do not lie on each other in overlapping intervals. This method is used in the experimental part and from the proposed method was found that studied GaAs and CdZnTe detectors do not have surface recombination.

Monte Carlo simulation including effects of diffusion, arbitrary electric field profile, two trap levels and initial distribution of carriers according to the absorption law and laser pulse shape is proposed to describe current waveforms. Pseudocode of MC simulation is presented. Two approximations of current waveforms beyond T_R for the detector with one shallow trap are derived. First approximation is for the shallow trap with the trapping time much smaller than T_R. Shallow trap causes trap controlled mobility, and effectively decreases carrier drift mobility and creates effective diffusion. Second approximation is for a weak shallow trap in which the trapping time is much larger than T_R. In this case some carriers are trapped/detrapped only once and rest of them are never trapped. Carriers separation into two groups produces discontinuity in current waveform at time T_R, after which exponential decay of current occurs. Applicability of these approximations is tested using MC simulation and discussed.

In experimental part GaAs and CdZnTe detectors are tested using spectroscopic measurements with $\alpha-$particles. In GaAs detector strong plasma effect prevents $\mu\tau$ product evaluation while in CdZnTe detector plasma effect is negligible and $(\mu\tau)_\alpha = 2 \cdot 10^{-3}$ cm^2/V is found. L-TCT technique is used with pulsed bias, which completely removes the space charge in both GaAs and CdZnTe detectors. From current waveforms of unpolarized detector transport parameters are evaluated using MC simulation. Excellent agreement of measured data and MC simulation of current waveforms is found for both types of detectors. Using evaluated parameters of unpolarized detector electric field profiles of polarized detector with DC bias are found. In GaAs detector increasing electric field profile from the cathode to the center of the detector, after which the electric field decreases to the anode is found. This electric field profile might be explained by variable conductivity in the detector material, which cannot be verified using only L-TCT and other measurements have to be used. In CdZnTe detector linear electric field profile decreasing from the cathode to the anode is found. This profile is caused by the presence of constant positive space charge inside the

whole detector at all applied DC biases. Electron drift mobility, initial photo-generated charge, trapping/detrapping time of shallow trap and trapping time of deep trap were also evaluated using MC simulation of L-TCT current waveforms for GaAs and CdZnTe detectors. Some transport parameters can also evaluated from spectroscopic measurements for CdZnTe detector while for GaAs detector transport parameter cannot be evaluated. In CdZnTe detector $(\mu\tau)_{LTCT}$ product evaluated from L-TCT measurements and $(\mu\tau)_{\alpha}$ product evaluated from spectroscopic measurements are the same. This further proves the usefulness of L-TCT, from which more transport parameters can be evaluated than from spectroscopic measurements.

In GaAs detector the effects of space charge limited currents are demonstrated using above bandgap LED illumination of detector cathode. Formation of the inactive layer (where electric field is almost zero) using LED illumination of detector anode is also demonstrated.

In future study, temperature dependence of current waveforms could be used to evaluate all parameters of traps, such as capture cross section, trap energy and concentration. Laser pulse mapping with various wavelength illumination of detector electrode can be used to study spatial dependence of space charge, transit time and charge collection. MC simulation is planned to be extended with carrier-carrier coulomb interaction.

A. Appendix

A.1 Exponential electron cloud

Let's assume the exponential charge distribution

$$n(x,t) = \frac{n_0}{x_d}\,\Theta(t)\exp\left(\frac{x-v_0t}{x_d}\right)\Theta(v_0t-x)\chi_{[0,L]}(x), \tag{A.1}$$

where $v_0 = \mu_e\mathcal{E}_0$ is the drift velocity, x_d is the characteristic length of electron cloud and the term $\Theta(v_0t-x)$ represents the front of the electron cloud. The charge distribution (A.1) is a solution of one dimensional transport equation (2.9). The exponential electron cloud is shown in figure A.1. The current waveform can be obtained from the Shockley-Ramo theorem (2.8) in analogical way to section 2.4

$$I(t) = \frac{Q_0}{T_R}\,\Theta(t)\frac{1}{x_d}\int_0^L \exp\left(\frac{x-v_0t}{x_d}\right)\Theta(v_0t-x)\mathrm{d}x. \tag{A.2}$$

Using substitution $y = x - v_0t, dy = dx$ we get

$$\int_{-v_0t}^{L-v_0t} \exp\left(\frac{y}{x_d}\right)\Theta(-y)\mathrm{d}y. \tag{A.3}$$

From (A.3) the current waveform is

$$I(t) = \frac{Q_0}{T_R}\,\Theta(t)\left[\exp\left(\frac{\min(L-v_0t,0)}{x_d}\right) - \exp\left(\frac{-v_0t}{x_d}\right)\right]. \tag{A.4}$$

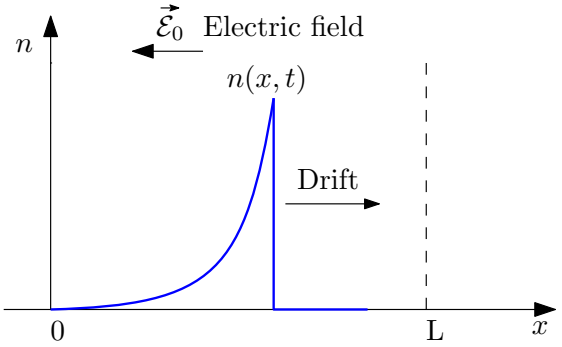

Figure A.1: Exponential electron cloud.

It is convenient to define τ_d

$$\frac{x_d}{L} = \frac{\tau_d}{T_R}, \tag{A.5}$$

where τ_d is the characteristic time of the exponential electron cloud that corresponds to its characteristic length x_d. Equation (A.5) comes from equation for constant drift velocity $x = v_0t$. Equation (A.4) can be further rewritten using equation (A.5) and $v_0 = L/T_R$ into

$$I(t) = \frac{Q_0}{T_R}\,\Theta(t)\exp\left(-\frac{t}{\tau_d}\right)\left[\exp\left(\frac{\min(1,t/T_R)}{\tau_d/T_R}\right) - 1\right]. \tag{A.6}$$

From (A.6) it is evident that for time $t > T_R$ the argument of the second exponential function in (A.6) is time independent and current waveform is exponentially decaying. Normalized current waveforms are shown in figure A.2, where red curve corresponds to the current waveform (2.16) of the delta function electron cloud and blue curve corresponds to the exponential electron cloud (A.6).

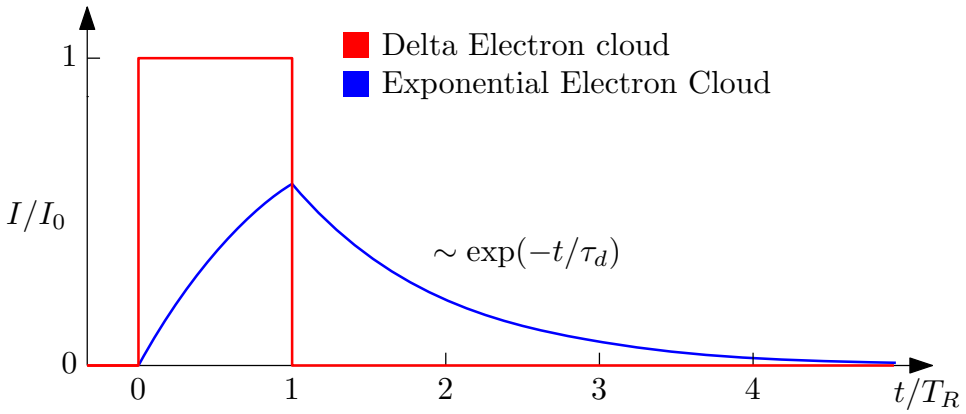

Figure A.2: Example of a normalized current waveform of the sample for initial delta function electron cloud (red curve) and exponential electron cloud (blue curve). Since there is no trapping total area under both curves is equal.

Bibliography

[1] Glenn F. Knoll. *Radiation Detection and Measurement*. John Wiley & Sons, 2010.

[2] C. Canali, M. Martini, G. Ottaviani, A. Alberigi Quaranta, and K. R. Zanio. Characterization of high resistivity CdTe for gamma-ray detectors. *Nuclear Instruments and Methods*, 96(4):561–571, nov 1971.

[3] S. J. Moss and A. Ledwith. *Chemistry of the Semiconductor Industry*. Springer Netherlands, 1989.

[4] M. C. Veale, S. J. Bell, D. D. Duarte, M. J. French, A. Schneider, P. Seller, M. D. Wilson, A. D. Lozinskaya, V. A. Novikov, O. P. Tolbanov, A. Tyazhev, and A. N. Zarubin. Chromium compensated gallium arsenide detectors for X-ray and gamma-ray spectroscopic imaging. *Nuclear Instruments and Methods in Physics Research Section A: Accelerators, Spectrometers, Detectors and Associated Equipment*, 752:6–14, jul 2014.

[5] T. E. Schlesinger and Ralph B. James. *Semiconductors for Room Temperature Nuclear Detector Applications*, volume 43. of *Semiconductors and Semimetals*. Elsevier Science, 1995.

[6] R. M. Blakney and H. P. Grunwald. Small-Signal Current Transients in Insulators with Traps. *Physical Review*, 159(3):658–664, jul 1967.

[7] Wayne E. Tefft. Trapping Effects in Drift Mobility Experiments. *Journal of Applied Physics*, 38(13):5265–5272, dec 1967.

[8] G. Ottaviani, C. Canali, C. Jacoboni, A. Alberigi Quaranta, and K. Zanio. Hole mobility and Poole-Frenkel effect in CdTe. *Journal of Applied Physics*, 44(1):360–371, jan 1973.

[9] R. Grill, E. Belas, J. Franc, M. Bugar, Š. Uxa, P. Moravec, and P. Hoschl. Polarization Study of Defect Structure of CdTe Radiation Detectors. *IEEE Transactions on Nuclear Science*, 58(6):3172–3181, dec 2011.

[10] Kazuhiko Suzuki, Takayuki Sawada, and Kazuaki Imai. Effect of DC Bias Field on the Time-of-Flight Current Waveforms of CdTe and CdZnTe Detectors. *IEEE Transactions on Nuclear Science*, 58(4):1958–1963, aug 2011.

[11] S. M. Sze. *Physics of semiconductor devices*. J. Wiley and Sons, 1969.

[12] Murray A. Lampert. Simplified Theory of Space-Charge-Limited Currents in an Insulator with Traps. *Physical Review*, 103(6):1648–1656, sep 1956.

[13] Lino Reggiani, editor. *Hot-Electron Transport in Semiconductors*. Springer Berlin Heidelberg, 1985.

[14] W. Shockley. Currents to Conductors Induced by a Moving Point Charge. *Journal of Applied Physics*, 9(10):635–636, oct 1938.

[15] Prem K. Kythe. *Fundamental Solutions for Differential Operators and Applications*. Birkhäuser Boston, 1996.

[16] G. Bertolini and A. Coche. *Semiconductor Detectors*. Elsevier Science, 1968.

[17] David J. Griffiths. *Introduction to Electrodynamics*. Cambridge University Pr., 2017.

[18] Štěpán Uxa, Roman Grill, and Eduard Belas. Evaluation of the mobility-lifetime product in CdTe and CdZnTe detectors by the transient-current technique. *Journal of Applied Physics*, 114(9):094511, sep 2013.

[19] A. Musiienko, R. Grill, J. Pekárek, E. Belas, P. Praus, J. Pipek, V. Dědič, and H. Elhadidy. Characterization of polarizing semiconductor radiation detectors by laser-induced transient currents. *Applied Physics Letters*, 111(8):082103, aug 2017.

[20] Štepán Uxa, Eduard Belas, Roman Grill, Petr Praus, and Ralph B. James. Determination of Electric-Field Profile in CdTe and CdZnTe Detectors Using Transient-Current Technique. *IEEE Transactions on Nuclear Science*, 59(5):2402–2408, oct 2012.

[21] G. T. Wright. Mechanisms of space-charge-limited current in solids. *Solid-State Electronics*, 2(2-3):165–189, mar 1961.

[22] A. Santi, M. Zanichelli, G. Piacentini, M. Pavesi, A. Cola, and I. Farella. An original method to evaluate the transport parameters and reconstruct the electric field in solid-state photodetectors. *Applied Physics Letters*, 104(19):193503, may 2014.

[23] A. Levi, M. M. Schieber, and Z. Burshtein. Carrier surface recombination in HgI2 photon detectors. *Journal of Applied Physics*, 54(5):2472–2476, may 1983.

[24] Carlo Jacoboni and Lino Reggiani. The Monte Carlo method for the solution of charge transport in semiconductors with applications to covalent materials. *Reviews of Modern Physics*, 55(3):645–705, jul 1983.

[25] William H. Press, Saul A. Teukolsky, William T. Vetterling, and Brian P. Flannery. *Numerical Recipes 3rd Edition: The Art of Scientific Computing*. Cambridge University Pr., 2007.

[26] W. E. Spear. Drift mobility techniques for the study of electrical transport properties in insulating solids. *Journal of Non-Crystalline Solids*, 1(3):197–214, apr 1969.

[27] Don Lemons. *Introduction to Stochastic Processes in Physics*. John Hopkins University Press, 2002.

[28] Karl Hecht. Zum mechanismus des lichtelektrischen primärstromes in isolierenden kristallen. *Zeitschrift für Physik*, 77(3-4):235–245, mar 1932.

[29] Petr Praus, Eduard Belas, Jiri Bok, Roman Grill, and Jakub Pekarek. Laser Induced Transient Current Pulse Shape Formation in (CdZn)Te Detectors. *IEEE Transactions on Nuclear Science*, 63(1):246–251, feb 2016.

[30] A. Tyazhev, V. Novikov, O. Tolbanov, A. Zarubin, M. Fiederle, and E. Hamann. Investigation of the current-voltage characteristics, the electric field distribution and the charge collection efficiency in x-ray sensors based on chromium compensated gallium arsenide. In Arnold Burger, Larry Franks, Ralph B. James, and Michael Fiederle, editors, *Hard X-Ray, Gamma-Ray, and Neutron Detector Physics XVI*. SPIE, sep 2014.

List of Figures

List of Tables

List of Symbols and Abbreviations

α	absorption coefficient
$\chi_{[0,x_1]}(x)$	boxcar function (see its definition (2.5))
$\delta(x)$	Dirac delta function
$\mathrm{erf}\,(x)$	error function (see its definition (2.29))
$\eta(t)$	number of trapping/detrapping events in time t
$\Theta(x)$	Heaviside unit step function (see its definition (2.6))
λ	wavelength of light
$\mathcal{N}$	number of superparticles representing carriers in Monte Carlo simulation
$\mathcal{N}_0$	inital number of electrons in the conduction band
$\mathcal{T}$	absolute temperature
μ_e, μ_h	electron, resp. hole drift mobility
μ_{eff}	effective electron mobility
ρ	space charge density
σ_c	capture cross section of trap
τ_C	$\frac{1}{\tau_C} = \frac{1}{\tau_{TS}} + \frac{1}{\tau_{TD}} + \frac{1}{\tau_{DS}}$
τ_e	$\frac{1}{\tau_e} = \frac{1}{\tau_{TS}} + \frac{1}{\tau_{DS}}$
τ_t	$\frac{1}{\tau_t} = \frac{1}{\tau_{TS}} + \frac{1}{\tau_{TD}}$
τ_{DJ}	detrapping time of the J-th trap level
τ_{DS}, τ_{DD}	detrapping time of the shalow resp. deep trap level
τ_{TJ}	trapping time of the J-th trap level
τ_{TS}, τ_{TD}	trapping time of the shallow resp. deep trap level
ε_0	permittivity of vacuum
ε_r	relative permittivity
$\vec{\mathcal{E}}$	electric field intensity
$\vec{D}$	electric displacement field ($\vec{D} = \varepsilon_r \varepsilon_0 \vec{\mathcal{E}}$)

$\vec{j_e}$	electron current density
a	slope of the electric field
D_e	diffusion coefficient for electrons
D_{eff}	effective diffusion coefficient
e	elementary charge
E_C	energy of the conduction band edge
E_T	energy of the trap in the band-gap
E_V	energy of the valence band edge
GR	generation-recombination process
I	electric current
I_0	default current amplitude ($I_0 = \frac{Q_0}{T_R}$)
k_B	Boltzmann constant
L	detector thickness
n	electron concentration in the conduction band
N_C	effective density of states in the conduction band
n_S, n_D	electron concentration in the shallow resp. deep trap
N_T	trap concentration
Q	electric charge
Q_0	initial photogenerated charge ($Q_0 = -e\mathcal{N}$)
t	time
t_k	time of the k-th simulation step
T_R	default transit time (see its definition (2.13))
t_r	actual transit time
T'_R	effective transit time
U	electric bias
v_0	constant drift velocity ($v_0 = L/T_R$)
v_{th}	thermal velocity of carrier
W	position of the inactive layer
(e-h) pair	electron-hole pair

CCE	Charge Collection Efficiency
CdZnTe	Cadmium Zinc Telluride
FWHM	Full Width at Half Maximum
GaAs	Gallium Arsenide
I-V	Current-Voltage
L-TCT	Laser-Induced Transient Current Technique
MC	Monte Carlo
MCA	Multi-Channel Analyzer
SR	Surface Recombination
TCT	Transient Current Technique